Chemical Engineering Journal 459 (2023) 141521

Contents lists available at ScienceDirect

Chemical Engineering Journal

journal homepage: www.elsevier.com/locate/cej

Macroscale superlubricity and durability of *in situ* grown hydrogenated graphene coatings

Shuyu Fan [a], Shu Xiao [a,*], Songsheng Lin [b,*], Fenghua Su [a], Yifan Su [b], Paul K. Chu [c]

[a] School of Mechanical & Automotive Engineering, South China University of Technology, Guangzhou 510641, China
[b] The Key Lab of Guangdong for Modern Surface Engineering Technology, National Engineering Laboratory for Modern Materials Surface Engineering Technology, Institute of New Materials, Guangdong Academy of Sciences, Guangzhou 510651, China
[c] Department of Physics, Department of Materials Science and Engineering, and Department of Biomedical Engineering, City University of Hong Kong, Tat Chee Avenue, Kowloon, Hong Kong, China

ARTICLE INFO

Keywords:
Graphene
Macroscale superlubricity
Molecular dynamics simulation
In situ
Self-healing

ABSTRACT

Although macroscale superlubricity reduces the friction of graphene materials, industrial application has been limited to special environments or complex strain engineering. Herein, high-quality hydrogenated graphene coatings ($0 < I_D/I_G < 0.21$) are synthesized on industrial materials *in situ* by hot-filament chemical vapor deposition. The ball-on-disk friction tests demonstrate that the hydrogenated graphene coatings have superior lubricating properties and long service lifetime at a macro-load of 1 N and high sliding speed (0.6 m/s) under ambient conditions (23–25 °C, 50–55 %RH). The hydrogenated graphene coatings deposited with moderate hydrogen supplies show ultra-low friction and even localized superlubricity (~0.009) due to the critical factor of surface defect density. Long-term stability is observed after more than 24,840 laps. Molecular dynamics simulation is performed to explain the self-passivating and self-healing effects on the atomic level. The macroscale lubrication mechanism involves H atoms capturing carbon dangling σ-bonds. The high-quality and chemically inert graphene surface facilitates the formation of a thick solid tribofilm at the sliding contact interface. The chemisorbed H atoms on the graphene layer lead to continuous healing and stabilization of the defective structure during the macroscale friction test. Our new findings provide insights into the lubrication mechanism and reveal a new approach to achieving macroscale superlubricity and high durability for hydrogenated graphene coatings.

1. Introduction

Friction is important to mechanical systems because more than 23 % of the world's energy is consumed by friction and most components fail due to frictional loss [1,2]. Solid lubricants can better reduce friction and improve the energy efficiency under harsh conditions than liquid or grease lubricants [3–5]. 2D materials such as graphene have good chemical stability, high specific surface area, high in-plane strength, low interlaminar shear strength, and low friction rendering them suitable for lubrication [6–8]. The friction properties are closely related to the surface properties and structure of graphene and in order to attain superlubricity and long-term durability, graphene materials are usually modified.

Superlubricity can only be achieved on the nanoscale and microscale from perfect graphene materials [9] because structural deformation and defects in graphene adversely affect the superlubricity as the dimension reaches the macroscale [10,11]. Until recently, superlubricity has been observed on the macroscale only under conditions such as N_2 [12–15] and vacuum [16]. This is because physisorbed and/or chemisorbed species from the external environment precipitate on the sliding surface to increase the electrostatic attraction/repulsion or capillary force consequently degrading the superlubricity [17]. In general, industrial lubricants require a macroscopic contact area (≥mm × mm), macro-load (N), high sliding speed, and exposure to air [18]. Breakthrough in macroscale superlubricity has recently been reported under ambient conditions using a graphene-coated plate (GCP)/graphene-coated microsphere (GCS)/graphene-coated ball (GCB) system, but the 35 mN maximum load limits the application [19]. Macroscale superlubricity has been observed from the graphene/MoS_2/FL-C:H ternary composite at a high load of 15 N in the ambient environment [20]. However, the

* Corresponding authors.
E-mail addresses: xiaos@scut.edu.cn (S. Xiao), linsongsheng@gdinm.com (S. Lin).

https://doi.org/10.1016/j.cej.2023.141521
Received 27 October 2022; Received in revised form 17 December 2022; Accepted 17 January 2023
Available online 21 January 2023

system requires perfect graphene and complex strain engineering to achieve macroscale superlubricity and the mechanism is still unclear. Therefore, it is important to elucidate the macroscale superlubricity mechanism and verify the theoretical models.

The characteristics of macroscale superlubricity have not been studied as extensively as those of microscale friction pertaining to electron-phono coupling, puckering, and energy dissipation [21–23]. On the macroscale, there are two main friction mechanisms responsible for the ultra-low friction and long service life of graphene materials under special conditions. The first one is the formation of a graphene transfer film which prevents direct contact during sliding [24,25]. The second one is associated with durable macroscale lubricity that can be achieved in a hydrogen ambient due to the hydrogen passivation of dangling σ-bonds in defective graphene [26]. However, graphene does not have a super low friction coefficient and the origin of the friction coefficient influenced by hydrogen is not well understood.

The role of hydrogen passivation in reducing adhesion and friction has been studied for other carbon-based films such as diamond-like carbon (DLC) [27–29] and diamond films [30,31] and macroscale superlubricity has been achieved from hydrogenated DLC films in a high vacuum or under inert conditions. The important role of hydrogen suggests that hydrogenated graphene deposited using different hydrogen supplies may show different lubricity and durability. Hydrogenated graphene as a graphene derivative prepared by chemical surface modification has attracted tremendous attention in electronic, magnetic, and optical applications [32–34]. Atomic H can bond chemically with C atoms on the graphene surface to disrupt the sp^2 symmetry but does not affect the stability [35,36]. Charge accumulation between C and H atoms and adjustment of the interfacial charge distribution due to accumulation of hydrogen in the edges and cavities of graphene leads to surface passivation of hydrogenated graphene coatings [37,38]. Some previous studies on graphene coatings have demonstrated the potential of hydrogenated graphene coatings in significantly reducing the friction of coefficient [39] and friction force [40] and prolonging wear lifetime [26]. Moreover, the excellent friction and wear properties of hydrogenated graphene are closely related to the degree of hydrogenation [41]. Hence, the hydrogenated states such as hydrogen supplies in graphene may affect the interfacial structure and physical, chemical, and adhesion interactions which can determine the macroscale friction properties. In fact, hydrogen plays dual role in the *in situ* fabrication of hydrogenated graphene coatings by acting both as an activator of surface-bound carbon and an etching agent which controls the size and morphology of graphene defects [42–44]. However, the relationship between the hydrogen supplies and structure of hydrogenated graphene coatings, macroscale friction properties, and mechanism under a macro-load and at a high sliding speed in air are not fully understood.

Herein, hydrogenated graphene coatings are fabricated *in situ* on industrial materials and the structure, lubricity, and durability are assessed. The macroscale friction under a macro-load and at a high sliding speed in air is investigated systematically. Ni-Co catalytic layer is deposited on the cemented carbide substrate by electrochemistry and annealing and the hydrogenated graphene coatings are fabricated using different hydrogen supplies by hot filament chemical vapor deposition (HFCVD) without a post-transfer step. In addition to experiments, molecular dynamics (MD) simulation is performed to study the self-passivating and self-healing effects of the highly hydrogenated graphene coatings. The results provide insights into how to achieve superlubricity and high durability for industrial applications.

2. Experimental details

2.1. In situ fabrication of graphene coatings

The hydrogenated graphene coatings were prepared on the 19 × 19 × 6 mm^3 cemented carbide (WC-Co) substrate (purchased from Zhuzhou Cementer Carbide Cutting Tools Co., ltd.) with a catalytic layer. *In situ* fabrication of the hydrogenated graphene coatings is illustrated in Fig. 1a. The WC-Co substrate was polished with a diamond grinding disc to a mirror finish, cleaned with ethanol ultrasonically for 10 min, and dried by an inert gas. A nickel catalytic layer was then electroplated on the substrate in the watt nickel electroplating bath system (Table 1). The substrate was the working electrode and electrodeposition was conducted at a current density of 13.3 mA/cm^2 for 60 min at 55 °C. Prior to fabrication of the hydrogenated graphene coatings, the nickel-coated substrate was annealed in a tube furnace followed at 700 °C for 60 min and cooled at a rate of 10 °C/min to form the Ni-Co catalytic layer.

The samples were placed in the HFCVD (Carbon Competence, Austria) reactor as shown in Fig. 1b. A mixture of CH_4 and H_2 was introduced into the chamber as the carbon source to a working pressure of 1 mbar during deposition. The substrate-to-filament (two Ta wires suspended in parallel) distance was 10 mm and the carbon source was heated to 2,000 °C. Hydrogenated graphene was produced at a substrate temperature of 654 °C for 10 min. The hydrogenated graphene coatings were synthesized by the following steps [45]: (i) The active carbon sources and H atoms diffused and adsorbed onto the Ni-Co catalytic layer; (ii) The adsorbed active carbon sources and H atoms underwent the surface reaction leading to diffusion and accumulation in the interior of the Ni-Co layer; (iii) During cooling, the solubility of carbon and H in the Ni-Co layer decreases and they migrate to the surface of the Ni-Co layer giving rise to *in situ* segregation in the hydrogenated graphene coatings.

2.2. Characterization

The morphology of the coatings was characterized by field-emission scanning electron microscopy (SEM, SU8220) and atomic force microscopy (AFM, Dimension Edge) and the microstructure and composition of hydrogenated graphene coatings were examined by high-resolution transmission electron microscopy (HR-TEM, JEM-3200FS) equipped with energy-dispersive X-ray microanalysis (EDX). The phases of the Ni-Co layers were determined by X-ray diffraction (XRD, Smartlab; Cu-kα line at 0.154 nm) and the elemental concentrations and distributions were obtained by electron probe micro-analysis (EPMA, JXA-iHP200F) and energy-dispersive X-ray spectroscopy (EDS). Raman scattering (LabRAM HR) was conducted on the hydrogenated graphene coatings at an excitation wavelength of 532 nm (0.5 mW). The grain size distribution in the Ni-Co layer was determined on an SEM (Gemini 300) equipped with an electron backscattered diffraction (EBSD) detector. The chemical composition and structure were determined by X-ray photoelectron spectroscopy (XPS, ESCALAB 250xi) and Fourier transform infrared spectroscopy (FTIR, TENSOR27).

2.3. Tribological tests

The macro-scale friction and wear tests were performed in air at room temperature and ambient humidity (23–25 °C, 50–55 %RH) using a ball-on-disk type tribometer (UMT-Tribolab, Bruker) against a counterpart (Al_2O_3 ball of 6 mm diameter). The tests were conducted at a load of 1 N and high average rotation speeds of 1,146 rpm (or 0.6 m/s). The friction coefficients were determined three times and the lubrication model of the hydrogenated graphene coatings is depicted in Fig. 1c. The hydrogenated graphene transfer layers (referred to as "tribofilms") were easily smeared on the Al_2O_3 ball contact surface during the friction test thus preventing direct contact with the counterpart and shear occurred mainly between the original hydrogenated graphene coatings and tribofilms [46]. After the tribological tests, the morphology, chemical composition, and structure of the wear track on the substrate and wear scar on the Al_2O_3 balls were examined by SEM, EDS, and Raman scattering. The wear rate (W) of the coatings was calculated by Eq. (1):

$$W = \frac{V}{S \bullet F} = \frac{2\pi rA}{S \bullet F} \quad (1)$$

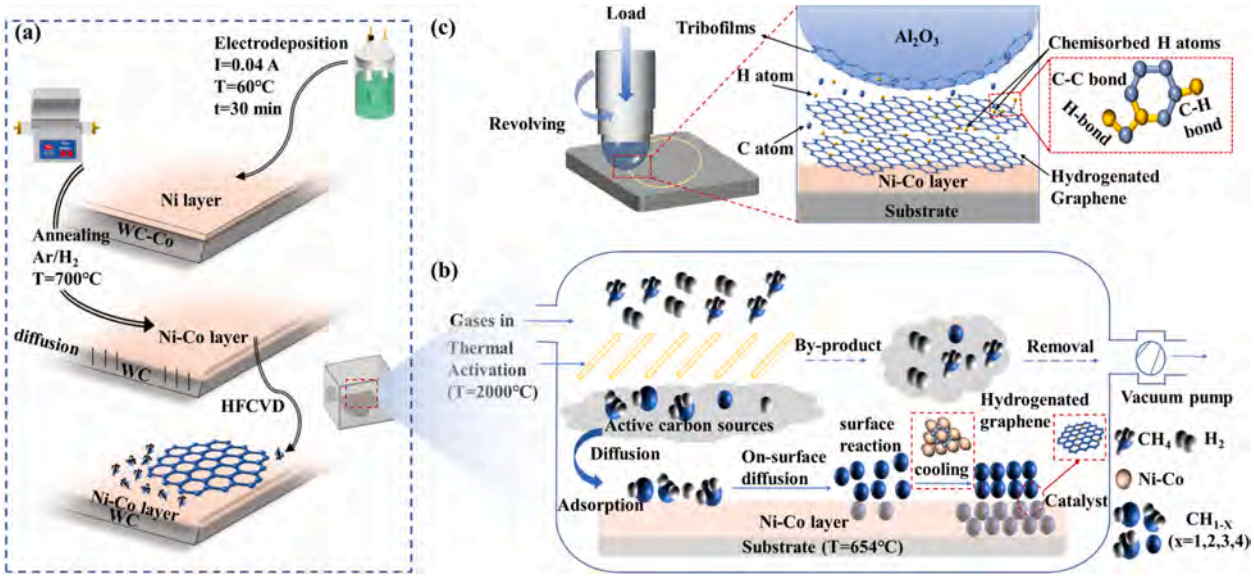

Fig. 1. Schematic illustrating the synthesis of hydrogenated graphene coatings and lubrication model. (a) Hydrogenated graphene fabrication process, (b) Hydrogenated graphene deposition principle in the HFCVD chamber, and (c) Lubrication model of hydrogenated graphene in the ambient environment.

Table 1
Watt nickel electroplating bath system.

Composition	Concentration
$NiSO_4{\cdot}6H_2O$	280 g/L
$NiCl_2$	16 g/L
H_3BO_3	32 g/L
$C_7H_5NO_3S$	0.4 g/L
$C_{12}H_{25}SO_4Na$	0.1 g/L

where r (mm), $A(mm^2)$, S (m), and F (N) are the wear radius, wear area, wear distance, and load, respectively. The wear track profile and wear area were measured by 3D profilometry (Dektak XT).

2.4. Molecular dynamics simulation

To analyze the tribological mechanism of the hydrogenated graphene coatings, molecular dynamics simulation was implemented in a large-scale atomic/molecular massively parallel simulator (Lammps) by the combination of reactive force-field (ReaxFF) [47] and charge equilibration method [48,49]. The total potential energy consisted of the bond energy, over coordination, undercoordination, long-pair, valence angle, torsion angle, van der Waals energy, and Coulomb energy in the ReaxFF as shown in Eq. (2):

$$E_{total} = E_{bond} + E_{over} + E_{under} + E_{lp} + E_{val} + E_{tors} + E_{vdWaals} + E_{Coulomb} \quad (2)$$

To calculate the charge distribution, the total electrostatic energy as shown in Eq. (3):

$$E_Q(Q_1 \ldots Q_N) = \sum_A \left(E_{A0} + X_A^0 Q_A\right) + 1/2 \sum_{A,B} Q_A Q_B J_{AB} \quad (3)$$

where J_{AB} is the Coulomb interaction between the unit charges on centers A and B and X_A^0 is a function of the charges on the atoms. The hydrogenated graphene was formed by stacking three graphene layers with a size of 138.7 Å along the *y-axis* and 100.1 Å along the *x-axis*. The defective hydrogenated graphene was formed by isothermal stretching, fracturing, releasing, and relaxing along the y direction at 326.85 °C. To confirm the effects of the different degree of hydrogenation on the atomic interactions in the sliding process, 15:1 and 5:1 ratios of C to H were set for the slightly and highly hydrogenation models. The hydrogenated graphene layers were relaxed at 326.85 °C for 2.5 ps and then cooled to −263.15 °C for hydrostatic simulation. The detailed molecular dynamics parameters are summarized in Table S1. The Al_2O_3 ball with a radius of 60 Å and a height of 10 Å was created by the Material Studio material library, which was subsequently balanced using H atoms and exported to the LAMMPS model with the help of msi2lmp software. Before hydrostatic calculation, the canonical ensemble (NVT) was selected to obtain a stable system at 326.85 °C and gradually cooled to −273.15 °C. In the simulation, the site was arranged along the set path and the adjacent site was spaced at 1 Å. The Al_2O_3 ball moved vertically downward in the rigid form at each site of the fixed hydrogenated graphene to find the minimum potential energy and the geometric configuration, charge, and potential energy were recorded. The periodic boundary conditions were applied in the *x*-axis and *y*-axis directions. The potential calculation path was $x = 0$ and $y = -30$–30 Å and the *z-axis* was the direction of control energy minimization.

3. Results and discussion

3.1. Fabrication and characterization of Ni-Co catalytic layer

To illustrate the fabrication steps of the Ni-Co catalytic layer on the WC-Co substrate, the schematic is displayed in Fig. 1(a). Firstly, the Ni catalytic layer is prepared by electrochemical deposition and then the Ni catalytic layer is annealed at a high temperature to promote diffusion of Co. When the annealing temperature exceeds the transition temperature of 417.25 °C for Co, the ε-Co simple hexagonal structure is transformed into an α-Co face-centered cubic (FCC) structure [50]. The morphology and elemental distribution are shown in Fig. S1a and b. The Ni-Co catalytic layer with a thickness of 13 μm covers the substrate uniformly. Moreover, there is strong bonding between the Ni catalytic layer and substrate and Co diffuses into the upper layer.

The Ni-Co layer grows tightly and continuously on the substrate and there is no obvious boundary at the interface (Fig. S1c). EDX reveals a relatively high Co concentration in the Ni-Co layer area (Fig. S1d–h) due to diffusion during annealing and hot filament deposition consistent with the EPMA result. The WC substrate shows the crystal plane of (10 $\bar{1}$ 1) and lattice spacing of 0.194 nm in Fig. S1i and the selected area electron diffraction (SAED) pattern of the substrate in Fig. S1j confirms the hexagonal close-packed (HCP) structure of WC. Fig. S1k shows that the Ni-Co layer has the ($\bar{1}$ 11) pane with a lattice spacing of 0.211 nm

and the SAED image in Fig. S1l indicates the FCC structure of Ni-Co layers in line with XRD. After annealing and hot filament deposition, due to the hcp structure of Co in the substrate being transformed into the same FCC structure, the small difference in the atomic size, electronegativity, and valence thus facilitates the formation of the Ni-Co substitutional solid solution at a high temperature [51].

The Ni-Co catalytic layer grains after annealing show the (1 1 1) plane mainly in conjunction with a few (2 0 0), (2 2 0), (3 1 1), and (2 2 2) planes (Fig. S2a). The XRD patterns of the substrate and Ni layer before annealing confirm the presence of WC, Co, and Ni phases, respectively (Fig. S2b) and c). The FWHM of (1 1 1) in the Ni-Co layer is narrower than that of the Ni layer before annealing, indicating that the grains are relatively large, but Scherrer's formula is no longer applicable for grain sizes exceeding 100 nm [52]. Therefore, EBSD is used to investigate the orientation and grain size of the Ni-Co catalytic layer. The Ni-Co grain size is larger than 1 μm and the grain size of 3–4 μm reaches 57.5 % (Fig. S2f and g). It has an fcc structure with an obvious texture on the (1 1 1), (1 1 0), and (1 0 0) planes as shown in Fig. S2d. Fig. S2e displays the inverse pole figure (IPF) with ⟨1 1 1⟩‖ ND being the dominant texture, which is a good match with the XRD results. The C atoms are mainly in the (1 1 1) plane matching the hexagonal lattice constants of hydrogenated graphene and the larger grain size facilitates the formation of hydrogenated graphene with fewer layers and orderly stacking [53]. However, Ni (1 1 0) and Ni (1 0 0) can grow on hydrogenated graphene with multilayered and disorderly stacking [54]. The last step not only forms substitutional the solid solution of Ni and Co but also increases the grain size and optimal orientation of the catalytic layer on the (1 1 1) plane. This is expected to enhance the adhesion strength and order of the hydrogenated graphene coatings.

3.2. Structural characterization of the hydrogenated graphene coatings

To study the effects of the hydrogen supplies on the chemical structure of the hydrogenated graphene coatings, FTIR is performed (Fig. 2a). The peak at 1622–1639 cm^{-1} corresponds to C=C of the hexagonal aromatic ring of the graphene sheet and the weak peak at 2872–2960 cm^{-1} reveals C-H stretching indicative of hydrogenated graphene [55,56]. After different hydrogenation, different bands of O-H (3215–3246 cm^{-1}), C=O (1714–1720 cm^{-1}), C-OH (1402–1412 cm^{-1}), and C-O (1026–1033 cm^{-1}) emerge indicating the role of hydrogen reduction [57]. When the hydrogen supplies are increased from 400 sccm to 1,500 sccm, the C=O, O-H, and C-OH peak intensity decreases but that of C-O increases. The presence of hydrogen-containing groups such as O-H and C-OH suggests adsorbed water on the surface of the sample [57,58]. The large hydrogen supply activates the Ni-Co catalytic layer for oxygen and adsorbed water removal from the surface by metal reduction [59]. Therefore, the content of hydrogen-containing groups decreases as the hydrogen supplies increase. In addition, there has a similar reduction between the hydrogenated graphene coatings deposited at 1,000 sccm and 1,500 sccm suggesting that the effects of increasing the hydrogen supplies on reduction decrease when the hydrogen supplies exceed 1,000 sccm.

XPS shows that the hydrogenated graphene coatings are composed of Ni, Co, O, and C as shown by the peaks at binding energies of 852.7 eV, 778.3 eV, 531.0 eV, and 284.5 eV attributed to Ni $2p_{3/2}$, Co $2p_{3/2}$, O 1 *s*, and C 1 *s*, respectively (Fig. S3). Fig. 2b–d display the XPS spectra of C 1 *s* fitted by the Lorentzian mode for sp^2-hybridized carbon. The dominant peak at 284.6 eV is related to C-C of graphene [60] and the peaks at 286.3 eV, 287.4 eV, and 283.1 eV are C-O, C=O, and NiC, respectively [61]. Since H cannot be detected by XPS, the hydrogenated graphene is determined indirectly by the degree of reduction [62]. At large hydrogen supplies, most of the C-O groups are removed by chemical reduction, leaving a few C-O groups consistent with FTIR. The oxygen-containing or NiC groups can be explained by incomplete or defective carbon bonds of hydrogenated graphene to which oxygen or Ni can bond during deposition [63]. Formation of NiC hinders epitaxial growth of hydrogenated graphene and causes more defects [64]. The defects also make the materials more disordered and reduce the modulus of elasticity and specific surface area [65,66].

To study the quality and hydrogenation degree, Raman scattering is carried out on the three samples (Fig. 2e and f). The dominant D peak at 1351 cm^{-1}, G peak at 1590 cm^{-1}, D' peak at 1630 cm^{-1}, and 2D peak at 2710 cm^{-1} are typical of hydrogenated graphene [67]. The peaks and full-width at half-maximum (FWHM) show a dependence on the hydrogen supplies. The D and D' peak represents the intervalley and intravalley double-resonance process at defects in graphene, which is an important feature of hydrogenated graphene and dominates in a range of hydrogen coverage [68]. The $I_D/I_{D'}$ and I_D/I_G ratios reveal that high edge defects are present in hydrogenated graphene coatings deposited at small hydrogen supplies. At hydrogen supplies less than 1,000 sccm, the dangling σ-bonds around the defects are partially saturated with H, but the excessive defect density leads to the loss of graphene surface area and reduces the hydrogen storage capacity consequently affecting the friction properties [69]. In highly hydrogenated graphene,

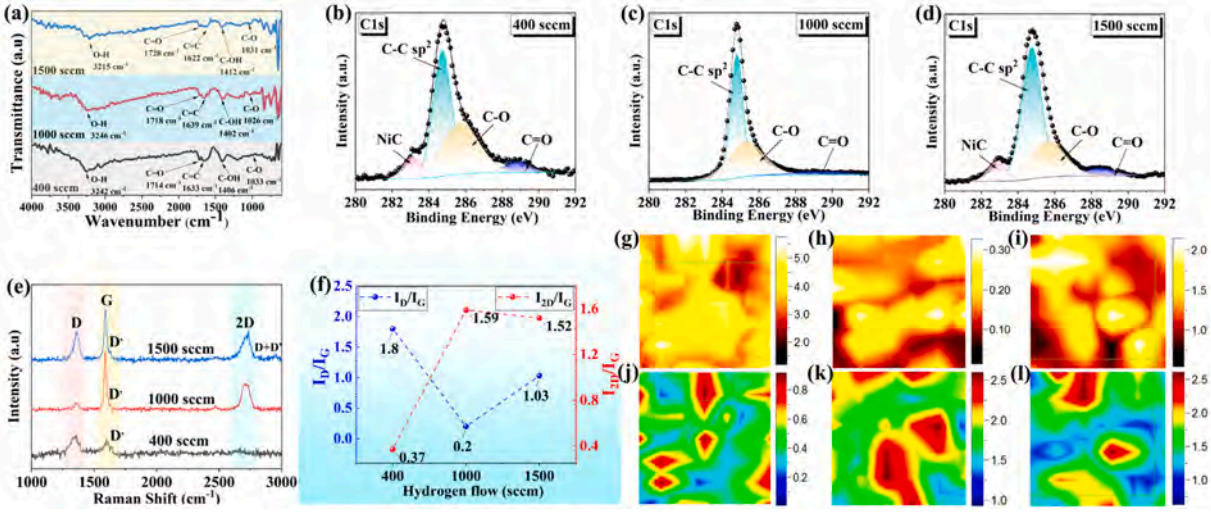

Fig. 2. Structural characterization of the hydrogenated graphene coatings deposited at different hydrogen supplies. (a) FTIR spectra. XPS C 1 *s* spectra of the samples deposited at (b) 400 sccm, (c) 1,000 sccm, and (d) 1,500 sccm. (e) Raman scattering spectra of the hydrogenated graphene. (f) Gaussian fitting of the Raman results. Raman maps for I_D/I_G of the samples deposited at hydrogen supplies of (g) 400 sccm, (h) 1,000 sccm, and (i) 1,500 sccm. Raman maps for I_{2D}/I_G of the samples deposited at (j) 400 sccm, (k) 1,000 sccm, and (l) 1,500 sccm.

electron–defect collisions affect in elastic scattering of electrons, and I_{2D}/I_G decreases with increasing hydrogen coverage [70]. At large hydrogen supplies over 1,000 sccm, owing to the coalescent defect cutting the long-range phonon interaction, D_{FWHM}, G_{FWHM}, $2D_{FWHM}$, and I_D/I_G increase with increasing hydrogen supplies during deposition, indicating higher hydrogen coverage in graphene. Moreover, hydrogenated graphene coating deposited at 1,500 sccm shows an additional D + D' peak at 2960 cm^{-1} which is a feature of hydrogen-terminated graphene caused by larger hydrogen supplies [71]. The Raman spectra Gaussian fitted parameters in Table S2 indicate that the catalytic layers play an important role in the growth and quality of hydrogenated graphene. Gaussian fitting and mapping are carried out in a 20 × 20 μm^2 area to investigate I_{2D}/I_G (complete coverage and number of graphene layers) and I_D/I_G (defect density) [42]. The I_{2D}/I_G value of 0.37 and I_D/I_G value of 1.8 for the film deposited at 400 sccm show the highest layer numbers and defect density, which corresponds to the map of I_{2D}/I_G (between 0.1 and 0.9, dominated by over 85 % light green color in Fig. 2j) and I_D/I_G (between 1 and 6, dominated by over 90 % by light yellow color in Fig. 2g). The hydrogenated graphene coating deposited at 1,500 sccm shows I_{2D}/I_G of 1.52 (mapping image containing a region of $0.5 < I_{2D}/I_G < 2.1$, agreeing with the features of few-layer as shown in Fig. 2l) and I_D/I_G of 1.03 (mapping image containing a region of $0.6 < I_D/I_G < 2.6$, as shown in Fig. 2i), indicating a decrease in the layer number and defect intensity. Fig. 3h presents the Raman mapping of I_D/I_G ($0 < I_D/I_G < 0.21$) of the hydrogenated graphene coating deposited at 1,000 sccm hydrogen and it is smaller than 1, suggesting generation of high-quality hydrogenated graphene coatings at moderate hydrogen supplies. Fig. 2k shows that the few-layer hydrogenated graphene ($1 < I_{2D}/I_G < 2.1$) has over 98 % of the total hydrogenated graphene coverage. As the flow rates go up from 400 sccm to 1,500 sccm (Fig. 2f), I_{2D}/I_G increases first and then decreases slightly. I_D/I_G which is positively related to defect density decreases initially and then increases with hydrogen supplies in line with the observation of oxygen or Ni bonds on the incomplete or defective carbon unraveled by XPS (Fig. 2b–d).

3.3. Morphological evolution of the hydrogenated graphene coatings

To investigate the morphological evolution of the hydrogenated graphene coatings deposited at hydrogen supplies from 400 sccm to 1,500 sccm, the SEM and AFM are performed (Fig. 3). Fig. 3a shows that the 400 sccm sample has the characteristics of amorphous carbon because the hydrogen supplies are not sufficient to remove excess C atoms giving rise to a significant amount of weakly bonded carbon (mostly amorphous) on the surface [72]. When the hydrogen coverage is low, the H atoms tend to attach to graphene to form clusters. Fig. 3b shows the image of the 1,000 sccm sample revealing continuous transparency and formation of an ultrathin film. In contrast, the 1,500 sccm specimen shows inhomogeneous patches and wrinkles after cooling (Fig. 3c) [73,74]. During cooling, the solubility of hydrogen increases and wrinkles are formed on the surface because of the expulsion of dissolved hydrogen from the substrate [75,76]. During high-temperature deposition, H_s is firstly activated and carbon species of $(CH_3)_s$ are formed from CH_4. $(CH_3)_s$ is successively dehydrogenated by H_s on the surface to generate more active carbon species $(CH_x)_s$ (x = 0,1, 2) further promoting growth. At the same time, the activated H_s controls the morphology by etching the weaker C-C bonds or forming C-H bonds. Therefore, hydrogen plays the dual role of a reducing reagent for strongly bonded carbon on the surface and an etching reagent to control the surface morphology of hydrogenated graphene [77].

$$Ni + H_2 \rightarrow 2H_s \quad (1)$$

$$(CH_4)_s + H_s \rightarrow (CH_3)_s + H_2 \quad (2)$$

$$(CH_x)_s + \text{graphene} \rightarrow (\text{graphene} + C) + H_2 \quad (3)$$

$$H_s + \text{graphene} \rightarrow \text{graphene-C} + (CH_x)_s \quad (4)$$

HFCVD performed at different hydrogen supplies produces hydrogenated graphene coatings with different roughness and wrinkle distribution are shown in Fig. 3d–f. As the hydrogen supplies go up, the roughness increases slightly as a result of structural transformation from the planar to three-dimensional tetrahedron due to hydrogenation. The

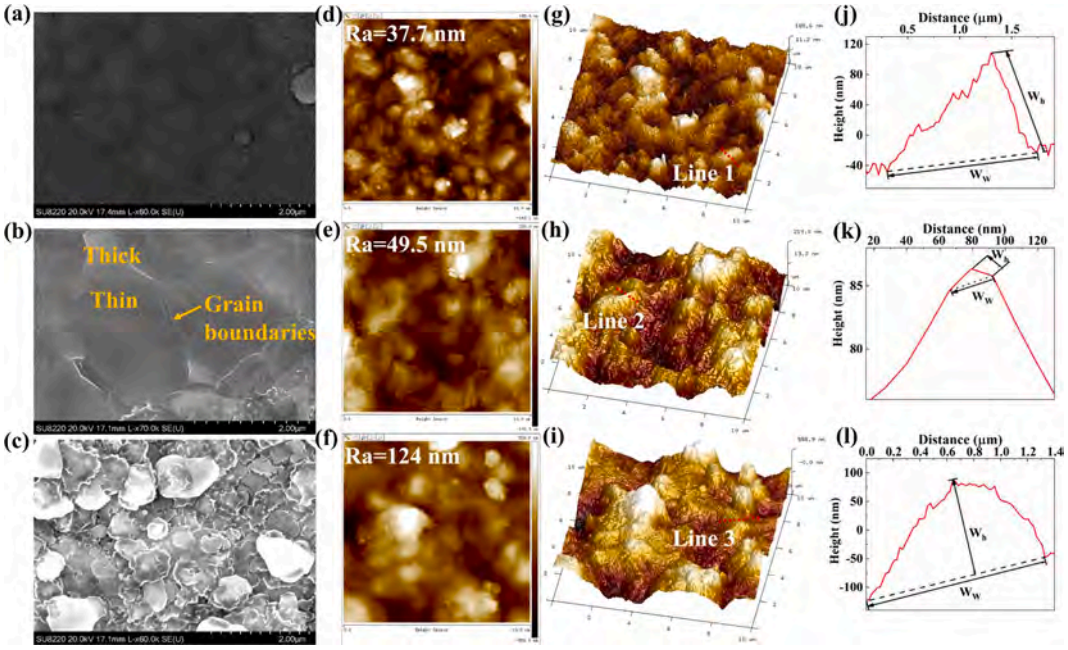

Fig. 3. Morphologies of the hydrogenated graphene coatings deposited at different hydrogen supplies. SEM images of the coatings deposited at (a) 400 sccm, (b) 1,000 sccm, and (c) 1,500 sccm. Two-dimensional topographic images taken from a 10 × 10 μm^2 area of the samples deposited at hydrogen supplies of (d) 400 sccm, (e) 1,000 sccm, and (f)1,500 sccm. Three-dimensional presentation of the 10 × 10 μm^2 area of the samples deposited at (g) 400 sccm, (h) 1,000 sccm, and (i)1,500 sccm. Height and width profiles of the wrinkles along the red line in the three-dimensional images of the samples deposited at (j) 400 sccm, (k) 1,000 sccm, and (l) 1,500 sccm. (For interpretation of the references to color in this figure legend, the reader is referred to the web version of this article.)

high roughness causes mechanical interlocking between their surface asperities resulting in high friction [78]. The wrinkles are shown in the three-dimensional figures (Fig. 3g–i) and the wrinkle widths and heights are presented in Fig. 3j–l. Ripples are shown in 1,000 sccm samples that W_h is less than 50 nm, while folded wrinkles are observed from the 400 sccm and 1,500 sccm samples [79]. The roughness and wrinkle morphology are slightly affected by the hydrogen supplies and expected to influence the friction properties slightly.

The hydrogenated graphene coatings deposited with large hydrogen supplies cover the Ni-Co catalytic layer, but the grey shade indicates uneven carbon layers in some regions (Fig. 3b, c). The low-magnification SEM image shows the presence of a small number of graphite layers, graphene grains, and graphene islands (Fig. S4) similar to Raman mapping (Fig. 2k, l) which reveals coverage of 98 % few-layer ($1 < I_{2D}/I_G$ less than 2.1) and 2 % multilayer (I_{2D}/I_G less than 1). Fig. 4 confirms partial heterogeneous coverage of hydrogenated graphene on the Ni-Co layer. The multilayer graphene area shows more than 10 layers presented in Fig. 4a. The region near the Ni-Co layer interface is orderly with a layer spacing of 0.393 nm, whereas the interlayer arrangement far from the Ni-Co layer interface is disorderly. Few-layer hydrogenated graphene coatings with 7–8 and 4–6 layers are shown in Fig. 4b and c, respectively. The lattice spacing is slightly larger than the theoretical thickness of single-layer graphene (0.34 nm) indicating that in-plane deformation occurs due to chemical modification [80]. The in-plane deformation of the graphene lattice causes interlayer interactions such that H atoms are cross-linked between layers by covalent bonds or chemisorbed. C is observed around Ni-Co, with a plane of (0 0 2) and lattice spacing of 0.393 nm as shown in Fig. 4d. The Moiré pattern with a twist angle of 6° is observed between the layers of hydrogenated graphene leading to the required incommensurate contact at the interface and responsible for the facile shearing and low friction. The inhomogeneous graphene layers indicate that the diffusion rate of carbon to the surface is determined by the rate of cooling, different grain sizes, and crystal orientation of the Ni-Co grains, but not the hydrogen supplies [81]. EBSD reveals that hydrogenated graphene is grown on the (1 1 1), (1 1 0), and (1 0 0) planes of the polycrystalline Ni-Co surface and there are different segregation rates for carbon. By considering the SEM, Raman mapping, and HRTEM results acquired from different hydrogenated graphene coatings, the *in situ* fabrication methods yield a nonuniform graphene layer in a wide thickness range, which is affected by the uneven grain size and grain orientation distribution of the polycrystalline Ni-Co layer. On the macroscale, as the frictional contact area increases, both the few-layer and multi-layer regions are contacted during sliding and so the thickness of graphene fabricated *in situ* may not be the main factor affecting the macroscale frictional performance. Therefore, hydrogen may affect the frictional performance mainly by influencing the surface defects, wrinkles, and roughness rather than the number of layers.

3.4. Tribological properties of the hydrogenated graphene coatings during short-duration sliding

To study the tribological properties of the hydrogenated graphene coatings for different hydrogen supplies, the relationship between the coefficients of friction (COF) and sliding laps is tested (Fig. 5a). Compared to the 400 sccm sample, the samples deposited at larger hydrogen supplies have smaller average COF. The 1,000 sccm sample shows a smaller average COF (0.021) than the other samples during sliding partially achieving superlubricity (~0.009). Good durability or lifetime is observed after 9,000 laps from the sample deposited at the largest hydrogen supplies. Hence, the protection and stability for lubrication require large hydrogen supplies. To verify the macroscale lubricity, comparative experiments are performed on the substrate and Ni-Co layer (Fig. S5(a)) which show large COFs of 1.908 and 0.490,

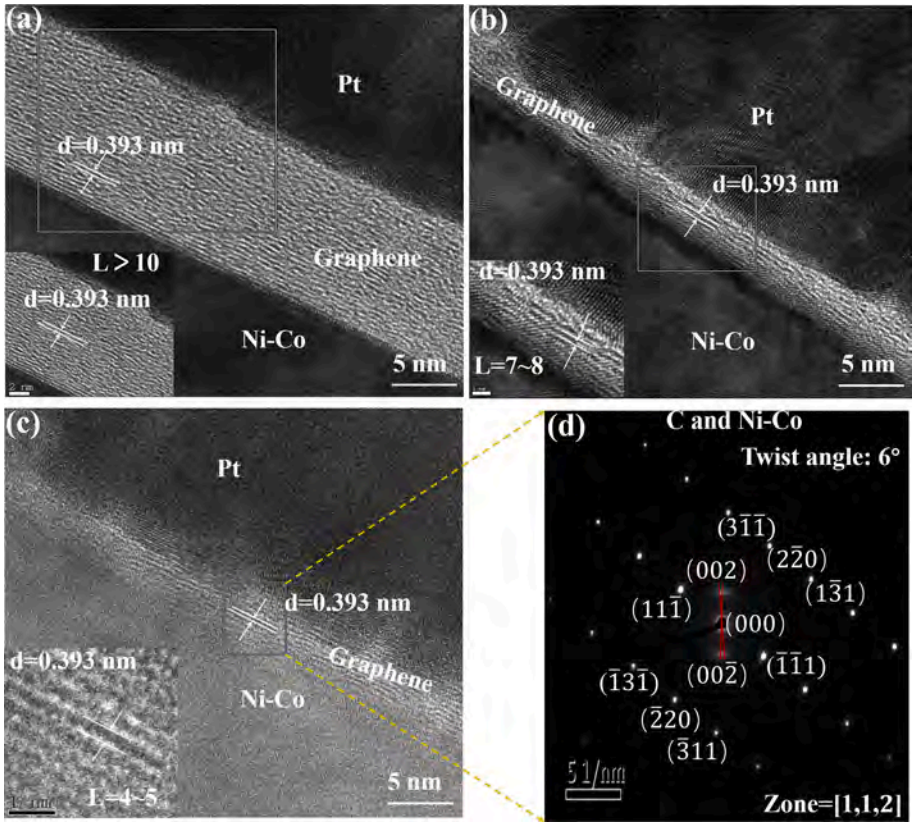

Fig. 4. HR-TEM images of the hydrogenated graphene coatings deposited using hydrogen supplies of 1,000 sccm: (a) Multilayer area and (b, c) Few-layer area. (d) SAED spectrum of the hydrogenated graphene and Ni-Co layer.

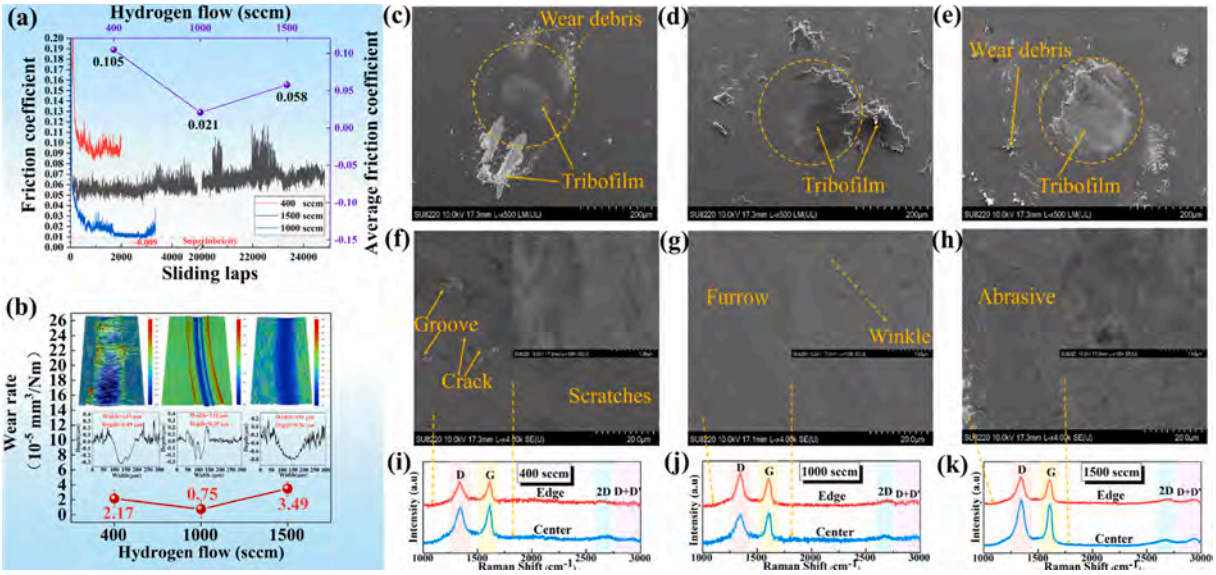

Fig. 5. Tribological properties of the hydrogenated graphene coatings deposited at different hydrogen supplies during short-duration sliding. (a) Coefficients of friction versus sliding laps and average coefficients of friction. (b) 3D morphologies, line scans, and wear rates of the wear track. Surface morphology of the wear scars on the counterpart balls for samples deposited at hydrogen supplies of (c) 400 sccm, (d) 1,000 sccm, and (e) 1,500 sccm. SEM images of the wear tracks on the samples deposited at hydrogen supplies of (f) 400 sccm, (g) 1,000 sccm, and (h) 1,500 sccm. Raman scattering spectra obtained from the center and edge of the wear track on the sample deposited at hydrogen supplies of (i) 400 sccm, (j) 1,000 sccm, and (k) 1,500 sccm.

respectively, which are 92 and 23 times higher than those of the 1,000 sccm sample. Investigation of lubrication mechanisms during short-duration sliding (955 laps) requires precise monitoring of the wear rate and wear behavior. Fig. 5b shows the 3D profiles, line scans, and wear rates of the wear tracks on the substrate lubricated by the hydrogenated graphene coatings. The hydrogenated graphene coatings reduce the wear rates from 3.49×10^{-5} to 0.75×10^{-5} mm^3/Nm. The wear tracks observed from the 400 sccm and 1,500 sccm samples are rough, wide (149 μm and 151 μm, respectively), and deep (0.49 μm and 0.56 μm, respectively). In comparison, the wear track on the 1,000 sccm sample is 110 μm wide and 0.29 μm deeply, thus showing the narrowest and shallowest furrows in agreement with Fig. 5a. The Raman mapping, HRTEM, and friction results show that there is no significant regularity in the macroscale frictional properties and thickness of hydrogenated graphene coatings. By considering the Raman and AFM results, the higher defects and roughness observed from the 400 sccm and 1,500 sccm specimens respectively reduce the lubricating properties and increase both the initial COFs and wear rates. Notably, compared with the trend of the initial roughness, the surface roughness of the hydrogenated graphene coatings decreases and shows a trend consistent with the friction of coefficient after short-duration sliding (Fig. S6). However, the measured roughness does not exhibit any discernable difference and therefore, the surface defect density is a more critical factor in controlling the friction of the hydrogenated graphene coatings than surface roughness. On the one hand, a large defect density reduces the specific surface area and increases the shear strength when the hydrogen supplies are low. On the other hand, large hydrogen supplies lead to shrinkage or rippling to increase the roughness slightly. The roughness increases slightly with the degree of hydrogenation, but the friction increase does not depend entirely on the roughness. It is more related to the effect of surface defect density than surface roughness. Therefore, the friction does not increase monotonically with the degree of hydrogenation. Fig. 5f reveals cracks, grooves, and scratches on the 400 sccm sample indicating plastic deformation. The 1,500 sccm sample is rougher and adhesive wear is observed as shown in Fig. 5h. The 1,000 sccm sample in Fig. 5g is smooth showing only small furrows and wrinkles (inset in Fig. 5g) boding well for superlubricity.

To elucidate the lubrication mechanisms of the hydrogenated graphene coatings, the counter-balls are characterized by SEM and Raman scattering from the edge and center of the wear track. The SEM image of the counter-balls reveals that after initial sliding, a tribofilm is formed in the contact area leading to indirect contact at the sliding interface as shown by the lubrication model in Fig. 1c. The tribofilms adhering to the surface of the counter-balls in Fig. 5c are thinner than those in Fig. 5d and e, and the friction increases as the tribofilms become thinner. The smooth, uniform, and thick tribofilms cover the counter surface as the hydrogen supplies are increased to 1,000 sccm and 1,500 sccm, which can prevent damaging the substrate and enhance lubrication. The ultra-low friction thus requires thick tribofilms which are absent from the substrate and Ni-Co layer without the hydrogenated graphene coatings (Fig. S5b-e). Fig. 5i–k shows an increase in D and a decrease in the 2D peak in the center and edge of the hydrogenated graphene compared to those before wear, which indicates a gradual loss of crystallinity and a higher defective and disordered nature. Moreover, I_D/I_G, which is positively correlated with structural defects decreases initially and then increases as the hydrogen supplies are increased from 400 sccm, 1,000 sccm to 1,500 sccm after the sliding test, and the structural defects in the center are larger than that in the edge region of wear track (Table S3). The new presence of D + D' peak suggests that chemisorbed H atoms at the interstices of graphene heal the hydrogenated graphene structure by constructing C-H bonds with the intrinsic stability, high dissociation energy, and chemical inertness which facilitate passivation and healing of defective graphene structures against disintegration. Meanwhile, Raman scattering indicates that graphene does not move away completely from the center and also accumulates at the edge of the wear track to enhance lubrication. During initial sliding, the hydrogenated graphene coatings are deformed so that graphene can be transported to the counter-balls and solid tribofilms are formed at the interface to prevent direct contact. The quality and integrity of the triboflims play a critical role in lubrication which depends on the initial quality (mainly defects, roughness, and wrinkles) of the hydrogenated graphene coatings. There are three possible routes in the model:

(A) There is not enough hydrogen to sustain the growth of hydrogenated graphene with good continuity and integrity. The largest defect density leads to low-quality tribofilms at the sliding interface and often gives rise to high shearing strength.

(B) Moderate hydrogenation shows excellent properties ($0 < I_D/I_G <$ 0.21) and smoothness yielding the maximum benefits in reducing friction.
(C) Expulsion of dissolved hydrogen during cooling by excessive hydrogen increases the defect density, roughness, and wrinkles adding to the friction.

3.5. Tribological properties of the hydrogenated graphene coatings in long-duration sliding

To determine the durability of the hydrogenated graphene coatings, longer sliding tests of more than 34,380 laps (1089 m) are performed in the air. The durability increases significantly with increasing hydrogen supplies, as demonstrated in Fig. 5a. The study of longer-duration sliding of hydrogenated graphene coatings is shown in Fig. S7. The 1,500 sccm sample lasts almost 24,840 laps or 780 m, whereas the 400 sccm and 1,000 sccm samples survive for 1,987 laps (62 m) and 3,344 laps (105 m), respectively, revealing the significant contributions of hydrogenation. By considering friction coefficients, the difference in the low friction and long durability is attributed to self-passivating and self-healing mechanisms caused by the surface properties and the stability of the internal structure of hydrogenated graphene coatings, respectively. Such passivating effects of hydrogen have been observed from hydrogenated diamond and diamond-like carbon films because the less unsaturated σ-bonds of C reduce friction [27,30]. The extended service life of the graphene coatings was reported to stem from hydrogen passivation of the dangling σ-bonds in broken graphene during the friction test in the H_2 [26]. However, in our work, the self-healing effect stabilizes the hydrogenated graphene coating structure and improves its durability at high sliding speeds under ambient conditions, which has not been reported before.

The wear scars on the counter-balls are shown in Fig. 6a–d after the long-duration sliding test. The wear debris is found from the edge but the tribofilms in the center are worn differently according to the short-duration test (Fig. 6b–d). The chemical composition of areas A, B, C, D, E, and F where the Al_2O_3 balls make contact or wear debris accumulated is shown in Fig. 6a, and C, O, Al, Co, Ni, and W are detected. The C, Al, and Ni concentrations in areas B, D, and F are larger than those in regions A, C, and F, indicating that wear debris originates from the graphene, Al_2O_3, and Ni layer. The Raman spectra of the Al_2O_3 balls exhibit hydrogenated graphene features at the edge of the wear scar, but not in the center (Fig. S8). Fig. 6f–h disclose different degrees of cracking, delamination, furrows, and wear debris. In particular, the 400 sccm sample shows the worst wear characteristics but the highly hydrogenated graphene coatings retain the stable structure despite the emergence of furrows. Another phenomenon observed from the chemical composition is that the decrease of C and increase of O and Ni are visible on the wear tracks, indicating more wear of hydrogenated graphene coatings and that lots of oxygen atoms adsorb during the long time friction (see Table S4 for details). There are not enough H atoms to react with C atoms at the defective edges on the slightly hydrogenated sample and almost no healing occurs, so that it cannot withstand the load during the long-term sliding test. The Raman spectra are displayed in Fig. 6i–k. The center of the wear track does not show a 2D peak (2710 cm^{-1}) and the graphene debris is pushed to the edge of the wear track in the form of amorphous carbon, thus increasing the friction. Moreover, I_D/I_G decreases first and then increases slightly with hydrogen supplies after long-duration sliding in line with the observation of the sample before sliding and after short-duration sliding (Table S3). This suggests that the structural defects in the hydrogenated graphene coatings decrease initially and then increase slightly with increasing hydrogen supplies after the sliding test. On the other hand, the highly hydrogenated samples show the new D + D' peaks at both the center and edge of the wear track, suggesting new interaction of C-H bonds caused by chemisorbed H atoms in interstices giving rise to healing of defects. Chemisorbed H atoms need to overcome an additional kinetic barrier to detach from the interstitial space between graphene layers and so multilayered graphene is more stable [74]. However, the defects decrease the surface area and hydrogen storage capacity.

Based on the experimental results, the mechanism is proposed as shown in Fig. 1c. H atoms bond strongly to C dangling σ-bonds when the hydrogen supplies are sufficient and some unbonded H atoms are present interstitially. The formation of CH bonds leads to a chemically inert surface with poor adhesion to the contact materials, thus providing

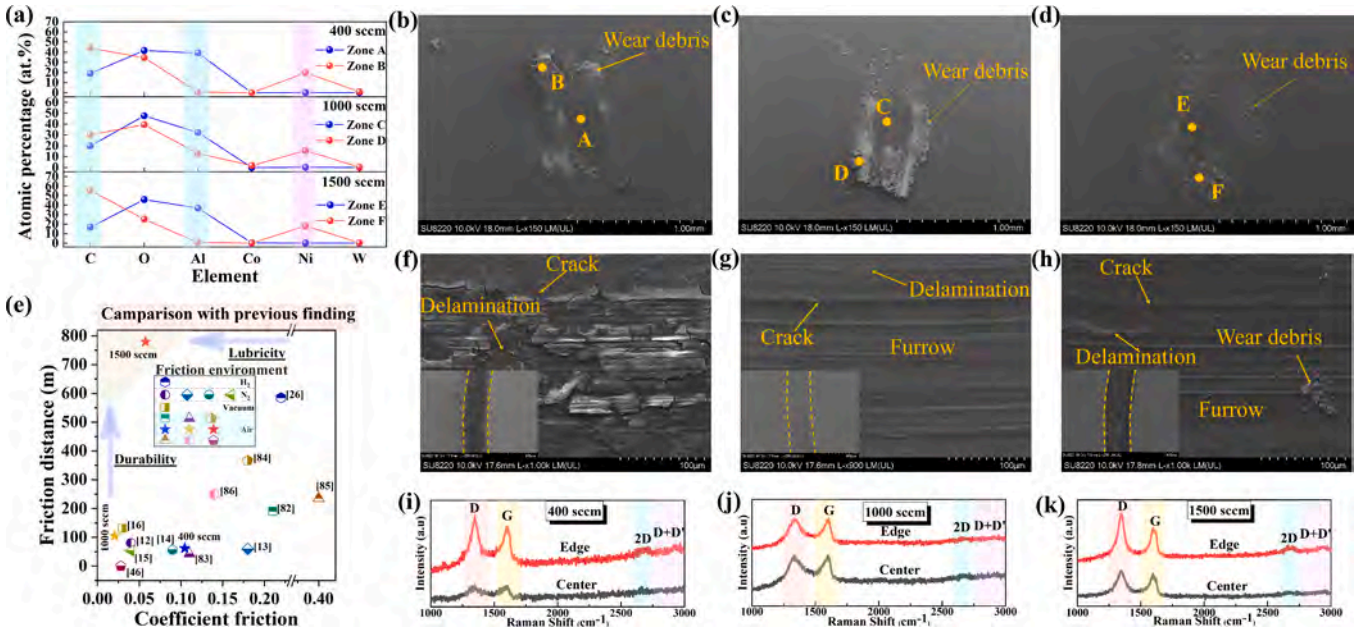

Fig. 6. Tribological properties of the hydrogenated graphene coatings deposited at different hydrogen supplies during long-duration sliding. (a) Chemical composition of the wear scars on the Al_2O_3 balls. Surface morphology of the wear scars on the Al_2O_3 balls for samples deposited at hydrogen supplies of (b) 400 sccm, (c) 1,000 sccm, and (d) 1,500 sccm. (e) Relationship between the friction distance and coefficient of friction revealed in this study and previous studies. SEM images of the wear tracks on sample deposited at hydrogen supplies of (f) 400 sccm, (g) 1,000 sccm, and (h) 1,500 sccm. Raman scattering spectra acquired from the center and edge of the wear track on the samples deposited at hydrogen supplies of (i) 400 sccm, (j) 1,000 sccm, and (k) 1,500 sccm.

structural stability during sliding. In addition, the chemisorbed H atoms in the hydrogenated graphene coatings continue to form new C-H bonds and heal the structure at the defect edges to improve the lifetime.

A small friction coefficient representing lubricity and long friction distances representing durability are critical to the macroscale friction applications of graphene materials. The friction properties of graphene materials in the air [46,82–86] or other environments such as H_2 [26], N_2 [12–15], and vacuum [16] and the relationship between the friction distance and COF have been studied (Fig. 6e). Either the lifetime is prolonged or the COF is reduced, but it has been difficult to accomplish both. However, compared to previous findings, the highly hydrogenated graphene coatings have both long-term durability (24,840 laps) and a small average COF. For example, the moderately hydrogenated sample shows a small average COF and partial superlubricity (~0.009) in addition to a long service lifetime in the air. The results provide guidance on how to achieve macroscale superlubricity and long-term durability for hydrogenated graphene coatings.

To explain the difference and reveal the link between the atomic-scale and macroscale friction behavior, molecular dynamics simulation is conducted to model the chemical interaction in the hydrogenated graphene layers deposited at different hydrogen supplies. Both the potential energy and charge field variation are calculated to characterize the C-H bond interactions and stability of the layers. In the model, an Al_2O_3 ball is placed on top of the hydrogenated graphene layers. The top ball moves downward by van der Waals force and the electric field force, which determines the lowest potential energy point. The calculated potential energy motion paths together with bonding and adsorption of H atoms (blue color) on C atoms (red color) on the two types of hydrogenated graphene layers are displayed in Fig. 7(a) and (b), respectively. Compared to the highly hydrogenated graphene layers, fewer H atoms chemisorb on the slightly hydrogenated graphene surface, and some dangling σ-bonds of C atoms at the graphene defects are not bound to form C-H bonds. The potential energy curves along the calculated paths ($y = -30$–30 Å) indicate an obvious enhancement of the potential in the defect range. There are still many dangling σ-bonds of C atoms on the surface giving rise to higher intermolecular forces and friction and therefore, the potential energy rises and reaches a maximum in the defect range (Fig. 7c and d). Weak interaction of H and C atoms on the slightly hydrogenated graphene surfaces leads to higher friction and wear [87]. By increasing the hydrogen supplies, the strong chemical bonding and adsorption interaction between H and C atoms occur at defective edges and interstices of graphene (Fig. 7b). In particular, H atoms prefer to bond the dangling σ-bonds of C atoms at the defective locations to form C-H bonds (Fig. 7e), as evidenced by the much lower potential energy at the defects in highly hydrogenated graphene layers (Fig. 7d). Hydrogen passivation stabilizes the hydrogenated graphene defective structure, thus reducing the molecular forces and friction during sliding, which can be derived from the total potential energy as being 13 % lower than that of the slightly hydrogenated graphene as well as lower potential energy at the defect range compared to defect-

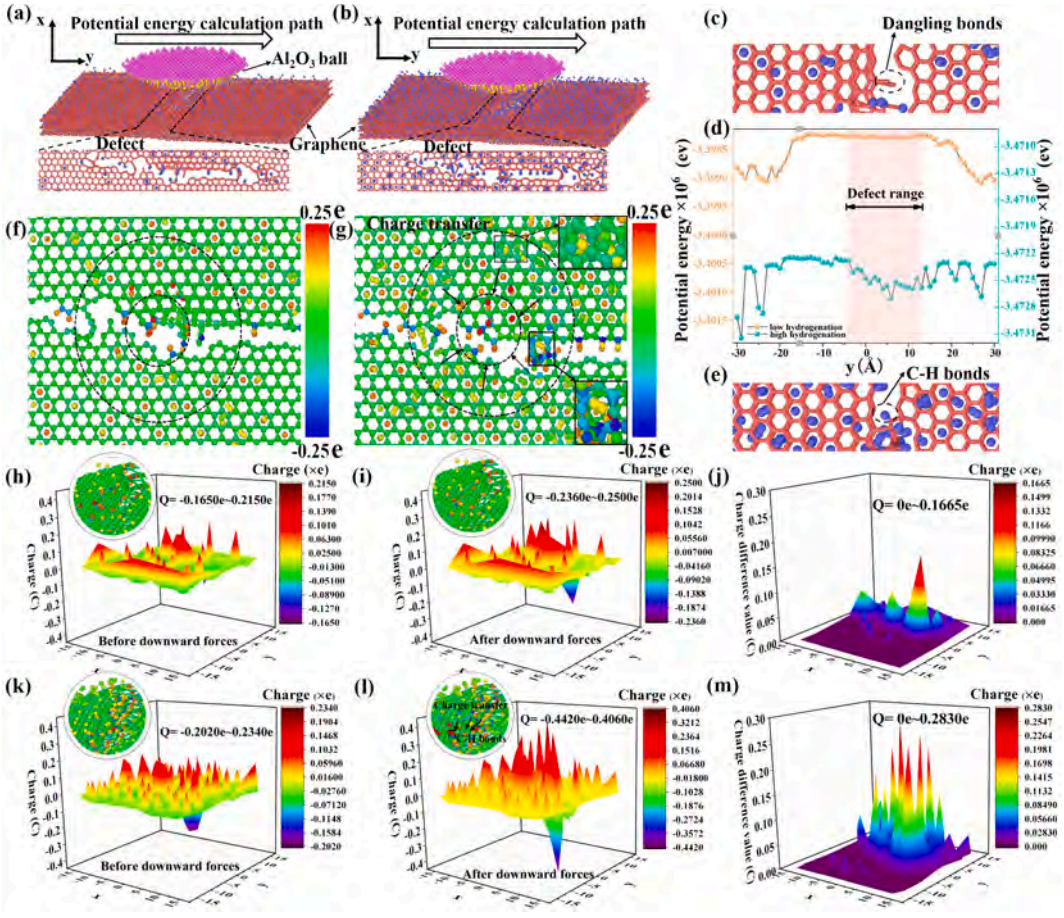

Fig. 7. Molecular dynamics simulation of different hydrogenated graphene layers. (a) Slightly hydrogenated graphene layers. (b) Highly hydrogenated graphene layers. (c) Calculated potential energy path in slightly hydrogenated graphene layers. (d) Potential energy as a function of position. (e) Calculated potential energy path in highly hydrogenated graphene layers. Charge distributions near the defect under the downward force: (f) Slightly hydrogenated graphene layers and (g) Highly hydrogenated graphene layers. Charge of slightly hydrogenated graphene layers in the range of $x = -15$–15 Å and $y = -15$–15 Å (h) before the downward force and (i) after the downward force. (j) Difference in the charge of slightly hydrogenated graphene layers before and after the downward force. Charge of highly hydrogenated graphene layers in the range of $x = -15$–15 Å and $y = -15$–15 Å (k) before the downward force and (l) after the downward force. (m) Difference in the charge of highly hydrogenated graphene layers before and after the downward force.

free locations in highly hydrogenated graphene. The chemisorbed H atoms occupying the reactive defect edges are responsible for the stability consistent with the experimental characterization such as Raman scattering (Figs. 2e, 5i–k, and 6i–k) and TEM (Fig. 4).

To obtain more information about the interactions between C and H atoms, charge calculation is performed for the coating-Al_2O_3 ball interactions (See Movie S1 and Movie S2). The highly hydrogenated graphene coatings (Fig. 7g) show a strong charge transfer interface in which C and H atoms interact with one another in comparison with the slightly hydrogenated graphene (Fig. 7f). As for the latter, the charge in the defective area ($x = -15$–15 Å, $y = -15$–15 Å) ranges from −0.1650e to 0.2150e before subjecting to the downward force (Fig. 7h), after which the charge changes in the range from −0.2630e to 0.2500e (Fig. 7i). The charge transition occurs in the interface before and after the downward force and the charge difference ranges from 0e to 0.1665e (Fig. 7j). However, the range of charges before and after the force is applied to the highly hydrogenated graphene layers is from −0.2020e to 0.2340e and from −0.4420e to 0.4060e, respectively (Fig. 7k and l). The difference is between 0e and 0.2830e, which is larger than that of the slightly hydrogenated graphene (Fig. 7m). The results show that the highly hydrogenated graphene layers allow chemisorbed H atoms to further form stronger C-H bonding networks under the downward force to heal the defective structure. At the coating-ball interface, charge transfer is the main contributor and the amount of charges changes. The chemisorbed H atoms in the hydrogenated graphene layers interact with the dangling σ-bonds of C and promote the formation of C-H bonds in the defective interface [88]. It can thus be concluded that C-H bonds are responsible for charge transfer and reduced potential energy. The C-H bonds have a high dissociation energy (410 kJ/mol) so that H and C atoms cannot dissociate easily from the hydrogenated graphene structure and thus serve to stabilize and heal the structure during mechanical contact. The new D + D' peaks after the friction test (Figs. 5i–k and 6i–k) provide evidence about the interaction between C and H atoms at the defective location and also explain the stability and durability.

4. Conclusions

In situ growth of hydrogenated graphene coatings with high quality ($0 < I_D/I_G < 0.21$) is demonstrated by HFCVD. Localized superlubricity (0.009) and ultra-long service life (24,840 laps) are achieved at a macro-load of 1 N and high sliding speed (0.6 m/s) under ambient conditions (23–25 °C, 50–55 %RH). Experiments and molecular dynamics simulation reveal the tribochemical mechanism at the contact interface and origin of the macroscale superlubricity and durability. H atoms are captured by carbon dangling σ-bonds at the defect edge and then form passivation tribofilms to prevent direct contact during sliding. The defect density is a more critical factor than surface roughness. The superlubricity does not increase monotonically with the hydrogen supplies and moderate hydrogenation produces the best outcome. Molecular dynamics simulation confirms potential energy reduction and charge transfer enhancement stemming from the strong C-H interactions. The chemisorbed H atoms in the highly hydrogenated graphene interstices passivate and heal the new C dangling σ-bonds giving rise to the enhanced durability. The self-passivating and self-healing effects rendered by the highly hydrogenated graphene coatings are responsible for the superlubricity and structural stability. The results reveal the mechanism and means to achieve macroscale superlubricity and high durability.

Declaration of Competing Interest

The authors declare that they have no known competing financial interests or personal relationships that could have appeared to influence the work reported in this paper.

Data availability

Data will be made available on request.

Acknowledgments

This work is supported by the National Natural Science Foundation of China (No. 52005187), Basic and Applied Basic Research Foundation of Guangdong Province (No.2019A1515110065), GDAS'Project of Science and Technology Development (No. 2022GDASZH-2022010109), City University of Hong Kong Donation Research Grant (DON-RMG No. 9229021), City University of Hong Kong Strategic Research Grant (SRG No. 7005505), as well as City University of Hong Kong Donation Grant (No. 9220061).

Appendix A. Supplementary data

Supplementary data to this article can be found online at https://doi.org/10.1016/j.cej.2023.141521.

References

[1] J.B. Lou, M. Liu, L.R. Ma, Origin of friction and the new frictionless technology-Superlubricity: advancements and future outlook, Nano Energy 86 (2021), 106092.
[2] K. Holmberg, A. Erdemir, Influence of tribology on global energy consumption, costs and emissions, Friction 5 (3) (2017) 263–284.
[3] D. Berman, A. Erdemir, A.V. Sumant, Graphene: a new emerging lubricant, Mater. Today 17 (1) (2013) 31–42.
[4] A. Rosenkranz, H.L. Costa, M.Z. Baykara, A. Martini, Synergetic effects of surface texturing and solid lubricants to tailor friction and wear-A review, Tribol. Int. 155 (2021), 106792.
[5] P. Wu, X.M. Li, C.H. Zhang, X.C. Chen, S.Y. Lin, H.Y. Sun, C.T. Lin, H.W. Zhu, J. B. Luo, Self-assembled graphene film as low friction solid lubricant in macroscale contact, ACS Appl. Mater. Interfaces 9 (25) (2017) 21554–21562.
[6] S.Z. Li, Q.Y. Li, R.W. Carpick, P. Gumbsch, X.Z. Liu, X.D. Ding, J. Sun, J. Li, The evolving quality of frictional contact with graphene, Nature 539 (7630) (2016) 541–546.
[7] L.C. Liu, M. Zhou, L. Jin, L.C. Li, Y.T. Mo, G.S. Su, X. Li, H.W. Zhu, Y. Tian, Recent advances in friction and lubrication of graphene and other 2D materials: mechanisms and applications, Friction 7 (3) (2019) 199–216.
[8] D. Berman, A. Erdemir, A.V. Sumant, Approaches for achieving superlubricity in two-dimensional materials, ACS Nano 12 (3) (2018) 2122–2137.
[9] W.Z. Zhai, K. Zhou, Nanomaterials in superlubricity, Adv. Funct. Mater. 29 (28) (2019) 1806395.
[10] O. Hod, E. Meyer, O.S. Zheng, M. Urbakh, Structural superlubricity and ultralow friction across the length scales, Nature 563 (7732) (2018) 485–492.
[11] J.S. Choi, J.S. Kim, I.S. Byun, D.H. Lee, M.J. Lee, B.H. Park, C. Lee, D. Yoon, H. Cheong, K.H. Lee, Y.W. Son, J.Y. Park, M. Salmeron, Friction anisotropy-driven domain imaging on exfoliated monolayer graphene, Science 333 (6042) (2011) 607–610.
[12] P.P. Li, P.F. Ju, L. Ji, H.X. Li, X.H. Liu, L. Chen, H.D. Zhou, J.M. Chen, Toward robust macroscale superlubricity on engineering steel substrate, Adv. Mater. 32 (36) (2020) 2002039.
[13] D. Berman, A. Erdemir, A.V. Sumant, Reduced wear and friction enabled by graphene layers on sliding steel surfaces in dry nitrogen, Carbon 59 (2013) 167–175.
[14] P.P. Li, L. Ji, H.X. Li, L. Chen, X.H. Liu, H.D. Zhou, J.M. Chen, Role of nanoparticles in achieving macroscale superlubricity of graphene/nano-SiO_2 particle composites, Friction 10 (9) (2022) 1305–1316.
[15] H. Song, L. Ji, H.X. Li, J.Q. Wang, X.H. Liu, H.D. Zhou, J.M. Chen, Self-forming oriented layer slip and macroscale super-low friction of graphene, Appl. Phys. Lett. 110 (7) (2017), 073101.
[16] D. Berman, S.A. Deshmukh, S.K.R.S. Sankaranarayanan, A. Erdemir, A.V. Sumant, Macroscale superlubricity enabled by graphene nanoscroll formation, Science 348 (6239) (2015) 1118–1122.
[17] A. Erdemir, Superlubricity and wear less sliding in diamondlike carbon films, Mater. Res. Soc. Symp. Proc. 697 (2002) 391–403.
[18] Z.Y. Cao, W.W. Zhao, A.M. Liang, J.Y. Zhang, A general engineering applicable superlubricity: hydrogenated amorphous carbon film containing nano diamond particles, ACS Appl. Mater. Interfaces 4 (14) (2017) 1601224.
[19] Z.Y. Zhang, Y.F. Du, S.L. Huang, F.N. Meng, L.L. Chen, W.X. Xie, K.K. Chang, C. H. Zhang, Y. Lu, C.T. Lin, Macroscale superlubricity enabled by graphene-coated surfaces, Adv. Sci. 7 (4) (2020) 1903239.
[20] R.Y. Li, C.J. Sun, X. Yang, Y.F. Wang, K.X. Gao, J.Y. Zhang, J.G. Li, Toward high load-bearing, ambient robust and macroscale structural superlubricity through contact stress dispersion, Chem. Eng. J. 431 (2022), 133548.
[21] R.J. Cannara, M.J. Brukaman, K. Cimatu, A.V. Sumant, S. Baldelli, R.W. Carpick, Nanoscale friction varied by isotopic shifting of surface vibrational frequencies, Science 318 (5851) (2007) 780–783.

[22] D.H. Cho, L. Wang, J.S. Kim, G.H. Lee, E.S. Kim, S.H. Lee, J. Hone, C.G. Lee, Effect of surface morphology on friction of graphene on various substrates, Nanoscale 5 (7) (2013) 3063.
[23] A. Smolyanitsky, J.P. Killgore, V.K. Tewary, Effect of elastic deformation on frictional properties of few-layer graphene, Phys. Rev. B. 85 (3) (2012), 035412.
[24] Y. Meng, F.H. Su, Y.Z. Chen, Supercritical fluid synthesis and tribological applications of silver nanoparticle-decorated graphene in engine oil nanofluid, Sci. Rep. 6 (2016) 31246.
[25] J.J. Li, T.Y. Gao, J.B. Luo, Superlubricity of graphite induced by multiple transferred graphene nanoflakes, Adv. Sci. 5 (3) (2018) 1700616.
[26] D. Berman, S.A. Deshmukh, S.K.R.S. Sankaranarayanan, A. Erdemir, A.V. Sumant, Extraordinary macroscale wear resistance of one atom thick graphene layer, Adv. Funct. Mater. 24 (42) (2014) 6640–6646.
[27] C.N. Bai, L.L. An, J. Zhang, X.K. Zhang, B. Zhang, L. Qiang, Y.L. Yu, J.Y. Zhang, Superlow friction of amorphous diamond-like carbon films in humid ambient enabled by hexagonal boron nitride nanosheet wrapped carbon nanoparticles, Chem. Eng. J. 402 (2020), 126206.
[28] J.D. Schall, G.T. Gao, J.A. Harrison, Effects of adhesion and transfer film formation on the tribology of self-mated DLC contacts, J. Phys. Chem. C 114 (12) (2010) 5321–5330.
[29] G.T. Gao, P.T. Mikulski, J.A. Harrison, Molecular-scale tribology of amorphous carbon coating: effects of film thickness, adhesion, and long-range interactions, J. Am. Chem. Soc. 124 (24) (2002) 7202–7209.
[30] A.V. Sumant, D.S. Grierson, J.E. Gerbi, J.A. Carlisle, O. Auciello, R.W. Carpick, Surface chemistry and bonding configuration of ultrananocrystalline diamond surfaces and their effects on nanotribological properties, Phys. Rev. B 76 (23) (2007), 235429.
[31] N. Kumar, R. Pamadoss, A.T. Kozakov, K.J. Sankaran, S. Dash, A.K. Tyagi, N.H. Tai, I.N. Lin, Humidity-dependent friction mechanism in an ultrananocrystalline diamond film, J. Phys. D. 46 (27) (2013), 275501.
[32] J. Son, S. Lee, S.J. Kim, B.C. Park, H.K. Lee, S. Kim, J.H. Kim, B.H. Hong, J. Hong, Hydrogenated monolayer graphene with reversible and tunable wide band gap and its field-effect transistor, Nat. Commun. 7 (2016) 13261.
[33] W.K. Lee, K.E. Whitener, J.T. Robinson, P.E. Sheehan, Patterning magnetic regions in hydrogenated graphene via E-Beam irradiation, Adv. Mater. 27 (10) (2015) 1774–1778.
[34] R.A. Schafer, J.M. Englert, P. Wehrfritz, W. Bauer, F. Hauke, T. Seyller, A. Hirsch, On the way to graphane-pronounced fluorescence of polyhydrogenated graphene, Angew. Chem. Int. Ed. 52 (2) (2013) 754–757.
[35] G.K. Sunnardianto, G. Bokas, A. Hussein, C. Walters, O.A. Moultos, P. Dey, Efficient hydrogen storage in defective graphene and its mechanical stability: a combined density functional theory and molecular dynamics simulation study, Int. J. Hydrogen Energy 46 (7) (2021) 5485–5494.
[36] D.C. Elias, R.R. Nair, T.M.G. Mohiuddin, S.V. Morozov, P. Blake, M.P. Halsall, A. C. Ferrari, D.W. Boukhvalov, M.I. Katsnelson, A.K. Geim, Control of graphene's properties by reversible hydrogenation: evidence for graphene, Science 323 (5914) (2009) 610–613.
[37] J.J. Wang, J.M. Li, L.L. Fang, Q. Sun, Y. Jia, Charge distribution view: large difference in friction performance between graphene and hydrogenated graphene systems, Tribol. Lett. 55 (3) (2014) 405–412.
[38] B.S. Pujari, S. Gusarov, M. Brett, A. Kovalenko, Single-side-hydrogenated graphene: density functional theory predictions, Phys. Rev. B. 84 (4) (2011), 041402.
[39] J.J. Wang, F. Wang, J.M. Li, S.J. Wang, Y.L. Song, Q. Sun, Y. Jia, Theoretical study of superlow friction between two single-side hydrogenated graphene sheets, Tribol. Lett. 48 (2) (2012) 225–261.
[40] G. Fessler, B. Eren, U. Gysin, T. Glatzel, E. Meyer, Friction force microscopy studies on $Si0_2$ supported pristine and hydrogenated graphene, Appl. Phys. Lett. 104 (4) (2014), 041910.
[41] D.L. Zhang, Z.B. Li, L.H. Klausen, Q. Li, M.D. Dong, Friction behaviors of two-dimensional materials at the nanoscale, Mater. Today Phys. 27 (2022), 100771.
[42] M.R. Anisur, P.C. Banerjee, C.D. Easton, R.K.S. Raman, Controlling hydrogen environment and cooling during CVD graphene growth on nickel for improved corrosion resistance, Carbon 127 (2017) 131–140.
[43] L. Lin, B. Deng, J.Y. Sun, H.L. Peng, Z.F. Liu, Bridging the gap between reality and ideal in chemical Vapor deposition growth of graphene, Chem. Rev. 118 (18) (2018) 9281–9343.
[44] Y.H. Zhang, Y.P. Sui, Z.Y. Chen, H. Kang, J. Li, S. Wang, S.W. Zhao, G.H. Yu, S. G. Peng, Z. Jin, X.Y. Liu, Role of hydrogen and oxygen in the study of substrate surface impurities and defects in the chemical vapor deposition of graphene, Carbon 185 (2021) 82–95.
[45] P. Wu, W. Zhang, Z. Li, J. Yang, Mechanisms of graphene growth on metal surfaces: theoretical perspectives, Small 10 (2014) 2136–2150.
[46] J.J. Li, X.Y. Ge, J.B. Luo, Random occurrence of macroscale superlubricity of graphite enabled by tribo-transfer of multilayer graphene nanoflakes, Carbon 138 (2018) 154–160.
[47] S. Hong, A.C.T. Van Duin, Atomistic-scale analysis of carbon coating and its effect on the oxidation of aluminum nanoparticles by ReaxFF-molecular dynamics simulations, J. Phys. Chem. C 120 (17) (2016) 9464–9474.
[48] A.K. Rappe, W.A. Goddard, Charge equilibration for molecular dynamics simulations, J. Phys. Chem. 95 (8) (1991) 3358–3363.
[49] A. Nakano, Parallel multilevel preconditioned conjugate-gradient approach to variable-charge molecular dynamics, Comput. Phy. Commun. 104 (1–3) (1997) 59–69.
[50] A. Sert, O.N. Celik, Characterization of the mechanism of cryogenic treatment on the microstructural changes in tungsten carbide cutting tools, Mater. Charact. 150 (2019) 1–7.
[51] N. Loudjani, T. Gouasmia, M. Bououdina, J.L. Bobet, Phase formation and magnetic properties of nanocrytalline Ni70Co30 alloy prepared by mechanical alloying, J. Alloys Compd. 846 (2020), 156392.
[52] A. Weibel, R. Bouchet, F. Boulc'h, P. Knauth, The big problem of small particles: A comparison of methods for determination of particle size in nanocrystalline anatase powders, Chem. Mater. 17 (9) (2005) 2378–2385.
[53] K.J. Shi, S. Xiao, Q.D. Ruan, H. Wu, G.H. Chen, C.L. Zhou, S.H. Jiang, K. Xi, M. H. He, P.K. Chu, Hydrogen permeation behavior and mechanism of multi-layered graphene coatings and mitigation of hydrogen embrittlement of pipe steel, Appl. Surf. Sci. 573 (2022), 151529.
[54] Y. Murata, V. Petrova, B.B. Kappes, A. Ebnonnasir, I. Petrov, Y.H. Xie, C. V. Ciobanu, S. Kodambaka, Moiré superstructures of graphene on faceted nickel islands, ACS Nano 4 (11) (2010) 6509–6514.
[55] B. Dischler, A. Bubenzer, P. Koidl, Bonding in hydrogenated hard carbon studied by optical spectroscopy, Solid State Commun. 48 (2) (1983) 105–108.
[56] M. Zhao, X.Y. Guo, O. Ambacher, C.E. Nebel, R. Hoffmann, Electrochemical generation of hydrogenated graphene flakes, Carbon 83 (2015) 128–135.
[57] V. Tucureanu, A. Matei, A.M. Avram, FTIR spectroscopy for carbon family study, Crit. Rev. Anal. Chem. 46 (6) (2016) 502–520.
[58] D.W. Chang, E.K. Lee, E.Y. Park, H. Yu, H.J. Choi, I.Y. Jeon, G.J. Sohn, D. Shin, N. Park, J.H. Oh, L.M. Dai, J.B. Baek, Nitrogen-doped graphene nanoplatelets from simple solution edge-functionalization for n-type field-effect transistors, J. Am. Chem. Soc. 135 (24) (2013) 8981–8988.
[59] H.U. Rashid, K.C. Yu, M.N. Umar, M.N. Anjum, K. Khan, N. Ahmad, M.T. Jans, Catalyst role in chemical vapor deposition (CVD) process: a review, Rev. Adv. Mater. Sci. 40 (3) (2015) 235–248.
[60] J.Y. Moon, M. Kim, S.I. Kim, S.G. Xu, J.H. Choi, D. Whang, K. Watanabe, T. Taniguchi, D.S. Park, J. Seo, S.H. Cho, S.K. Son, J.H. Lee, Conducting graphene synthesis from electronic waste, Sci. Adv. 6 (44) (2020) eabc6601.
[61] X.N. Chen, X.H. Wang, D. Fang, A review on C1s XPS-spectra for some kinds of carbon materials, Fuller. Nanotub. Carbon Nanostructures 28 (12) (2020) 1048–1058.
[62] K.E. Whitener, Review Article: Hydrogenated graphene: A user's guide, J. Vac. Sci. Technol. A 36 (5) (2018) 05G401.
[63] Z. Fogarassy, M.H. Rummeli, S. Gorantla, A. Bachmatiuk, G. Dobrik, K. Kamaras, L. P. Biro, K. Havancsak, J.L. Labar, Dominantly epitaxial growth of graphene on Ni (111) substrate, Appl. Surf. Sci. 314 (2014) 490–499.
[64] P. Jacobson, B. Stoger, A. Garhofer, G.S. Parkinson, M. Schmid, R. Caudillo, F. Mittendorfer, J. Redinger, U. Diebold, Nickel carbide as a source of grain rotation in epitaxial graphene, ACS Nano 6 (4) (2012) 3564–3572.
[65] R. Dettori, E. Cadelano, L. Colombo, Elastic fields and moduli in defected graphene, J. Phys. Condens. Matter 24 (10) (2012), 104020.
[66] M.H. Gass, U. Bangert, A.L. Bleloch, P. Wang, R.R. Nair, A.K. Geim, Free-standing graphene at atomic resolution, Nat. Nanotechnol. 3 (11) (2008) 676–681.
[67] J.B. Wu, M.L. Lin, X. Cong, H.N. Liu, P.H. Tan, Raman spectroscopy of graphene-based materials and its applications in related devices, Chem. Soc. Rev. 47 (5) (2018) 1822–1873.
[68] M.M. Lucchese, F. Stavale, E.H.M. Ferreira, C. Vilani, M.V.O. Moutinho, R. B. Capaz, C.A. Achete, A. Jorio, Quantifying ion-induced defects and Raman relaxation length in graphene, Carbon 48 (5) (2010) 1592–1597.
[69] H.G. Shiraz, O. Tavakoli, Investigation of graphene-based systems for hydrogen storage, Renew. Sust. Energy Rev. 74 (2017) 104–109.
[70] Z.Q. Luo, T. Yu, Z.H. Ni, S.H. Lim, H.L. Hu, J.Z. Shang, L. Liu, Z.X. Shen, J.Y. Lin, Electronic structures and structural evolution of hydrogenated graphene probed by Raman spectroscopy, J. Phys. Chem. C 115 (5) (2011) 1422–1427.
[71] Z.Q. Luo, T. Yu, K.J. Kim, Z.H. Ni, Y.M. You, S. Lim, Z.X. Shen, S.Z. Wang, J.Y. Lin, Thickness-dependent reversible hydrogenation of graphene layers, ACS Nano 3 (7) (2009) 1781–1788.
[72] Z.Z. Sun, Z. Yan, J. Yao, E. Beitler, Y. Zhu, J.M. Tour, Growth of graphene from solid carbon sources, Nature 468 (2010) 549–552.
[73] U. Bangert, C.T. Pan, R.R. Nair, M.H. Gass, Structure of hydrogen-dosed graphene deduced from low electron energy loss characteristics and density functional calculations, Appl. Phys. Lett. 97 (25) (2010), 253118.
[74] X. Zhang, Y. Huang, S.S. Chen, N.Y. Kim, W. Kim, D. Schilter, M. Biswal, B. Li, Z. Lee, S. Ryu, C.W. Bielawski, W.S. Bacsa, R.S. Ruoff, Birch-type hydrogenation of few-layer graphenes: products and mechanistic implications, J. Am. Chem. Soc. 138 (45) (2016) 14980–14986.
[75] L.B. Gao, W.C. Ren, J.P. Zhao, L.P. Ma, Z.P. Chen, H.M. Cheng, Efficient growth of high-quality graphene films on Cu foils by ambient pressure chemical vapor deposition, Appl. Phys. Lett. 97 (18) (2010), 183109.
[76] M. Losurdo, M.M. Giangregorio, P. Capezzuto, G. Bruno, Graphene CVD growth on copper and nickel: role of hydrogen in kinetics and structure, Phys. Chem. Chem. Phys. 13 (46) (2011) 20836–20843.
[77] I. Vlassiouk, M. Regmi, P.F. Fulvio, S. Dai, P. Datskos, G. Eres, S. Smirnov, Role of hydrogen in chemical vapor deposition growth of large single-crystal graphene, ACS Nano 5 (7) (2011) 6069–6076.
[78] W.J. Meng, A. Kumar, G.L. Doll, Y.T. Cheng, S. Veprek, Y.W. Chung, Superlubricity and wearless sliding in diamondlike carbon films, Surf. Eng. 697 (2001) 391–403.
[79] Z.P. Chen, W.C. Ren, L.B. Gao, B.L. Liu, S.F. Pei, H.M. Cheng, Three-dimensional flexible and conductive interconnected graphene networks grown by chemical vapour deposition, Nat. Mater. 10 (6) (2011) 424–428.

[80] Y.H. Xue, Q. Zhang, W.J. Wang, H. Cao, Q.H. Yang, L. Fu, Opening two-dimensional materials for energy conversion and storage: a concept, Adv. Energy Mater. 7 (19) (2017) 1602684.
[81] L. David, R. Bhandavat, G. Kulkarni, S. Pahwa, Z. Zhong, G. Singh, Synthesis of graphene films by rapid heating and quenching at ambient pressures and their electrochemical characterization, ACS Appl. Mater. Interfaces 5 (3) (2013) 546–552.
[82] D. Berman, A. Erdemir, A.V. Sumant, Few layer graphene to reduce wear and friction on sliding steel surfaces, Carbon 54 (2013) 454–459.
[83] H. Hong, S.L. Chen, X. Chen, Z.N. Zhang, B. Shen, F. Fang, Study on the friction reducing effect of graphene coating prepared by electrophoretic deposition, Proc. CIRP 71 (2018) 335–340.
[84] S. Singh, X.C. Chen, C.H. Zhang, R.K. Gautam, R. Tyagi, J.B. Luo, Nickel-catalyzed direct growth of graphene on bearing steel (GCr15) by thermal chemical vapor deposition and its tribological behavior, Appl. Surf. Sci. 502 (2020), 144135.
[85] J.H. Lee, S.H. Kim, D.H. Cho, S.C. Kim, S.G. Baek, J.G. Lee, J.M. Kang, J.B. Choi, C. S. Seok, M.K. Kim, J.C. Koo, B.S. Lim, Tribological properties of chemical vapor deposited graphene coating layer, Korean J. Mater. Res. 50 (3) (2012) 206–211.
[86] L. Xiang, Q.Q. Shen, Y. Zhang, W. Bai, C.Y. Nie, One-step electrodeposited Ni-graphene composite coating with excellent tribological properties, Surf. Coat. Technol. 373 (2019) 38–46.
[87] D. Yi, L. Yang, S.J. Xie, A. Saxena, Stability of hydrogenated graphene: a first-principles study, RSC Adv. 5 (26) (2015) 20617–20622.
[88] J.J. Wang, F. Wang, J.M. Li, S.J. Wang, Y.L. Song, Q. Sun, Y. Jia, Theoretical study of superlow friction between two single-side hydrogenated graphene sheets, Tribol. Lett. 48 (2) (2012) 255–261.

Supplementary Materials

Macroscale Superlubricity and Durability of *In Situ* Grown Hydrogenated Graphene Coatings

Shuyu Fan[1], Shu Xiao[1*], Songsheng Lin[2*], Fenghua Su[1], Yifan Su[2], Paul K. Chu[3]

[1] School of Mechanical & Automotive Engineering, South China University of Technology, Guangzhou 510641, China

[2] The Key Lab of Guangdong for Modern Surface Engineering Technology, National Engineering Laboratory for Modern Materials Surface Engineering Technology, Institute of New Materials, Guangdong Academy of Sciences, Guangzhou 510651, China

[3] Department of Physics, Department of Materials Science and Engineering, and Department of Biomedical Engineering, City University of Hong Kong, Tat Chee Avenue, Kowloon, Hong Kong, China

[*] Corresponding authors: xiaos@scut.edu.cn (S. Xiao); linsongsheng@gdinm.com (S.S. Lin)

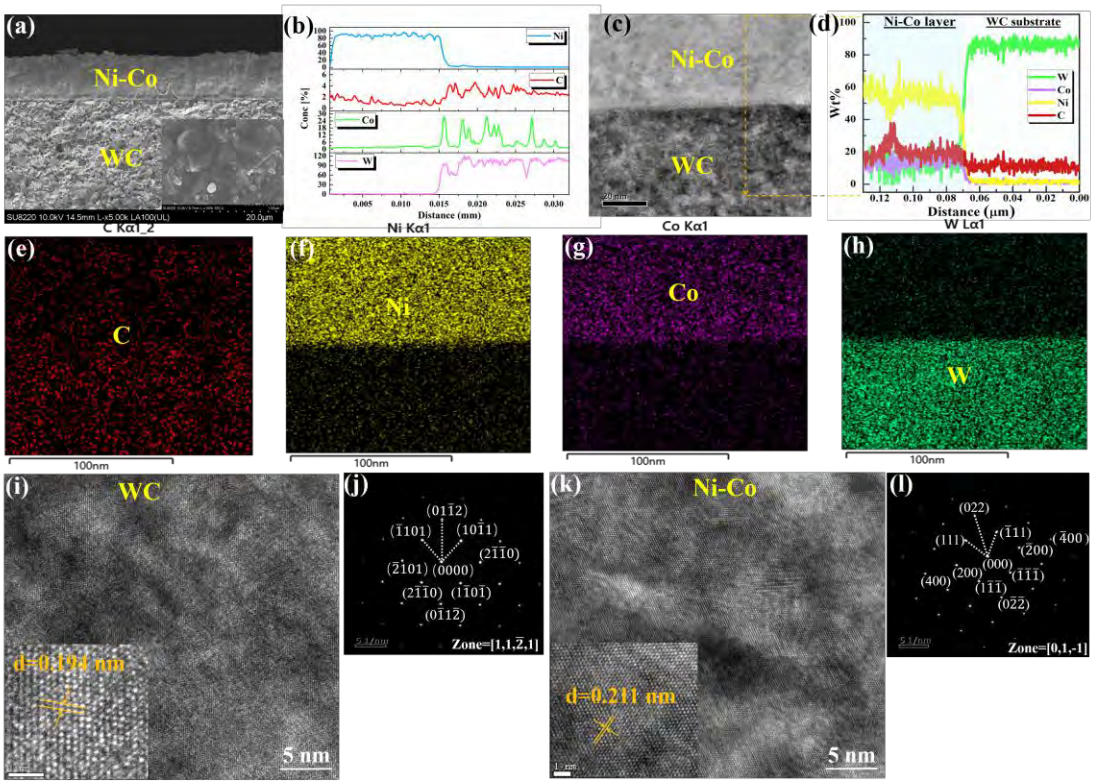

Fig. S1. Cross-sectional morphology and elemental characterization of the Ni-Co catalytic layer. (a) SEM cross-sectional and surface morphology (inset) of the Ni-Co layer. (b) EPMA line scans of the cross-section of the Ni-Co layer. (c) Cross-sectional TEM image of the Ni-Co layer and WC substrate interface. (d) EDX line scans and (e, f, g, h) elemental maps of the Ni-Co layer and WC substrate interface. (i, j) HR-TEM and SAED images of the WC substrate. (k, l) HR-TEM and SAED images of the Ni-Co layer.

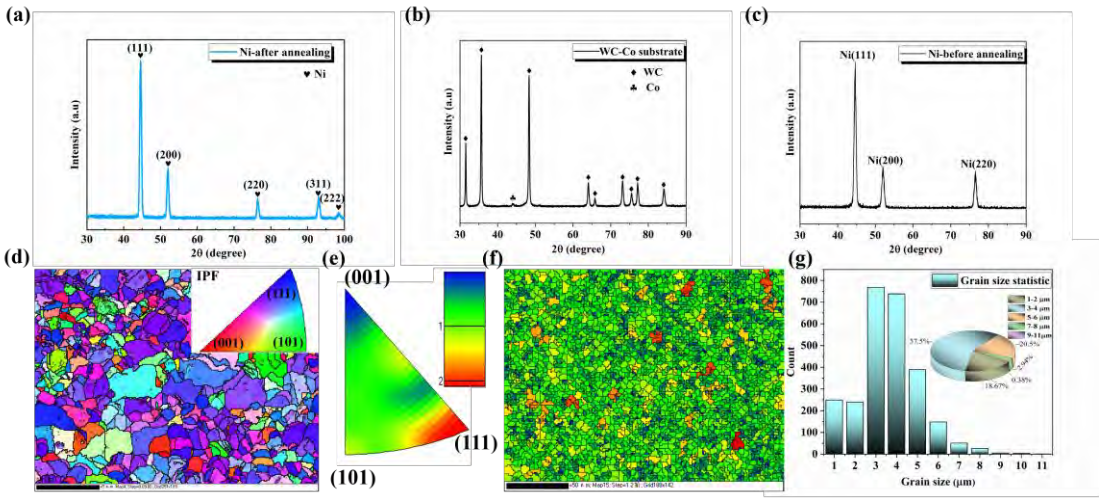

Fig. S2. Structural characterization of the Ni-Co catalytic layer. XRD patterns of (a) Ni layer after annealing, (b) WC-Co substrate, and (c) Ni layer before annealing. (d) IPF and grain size maps of the Ni-Co layer. (e) Inverse pole of Fig. S2(d) of the Ni-Co layer. EBSD grain size results of the Ni-Co layer in low magnification: (f) Grain size map and (g) Train size statistics.

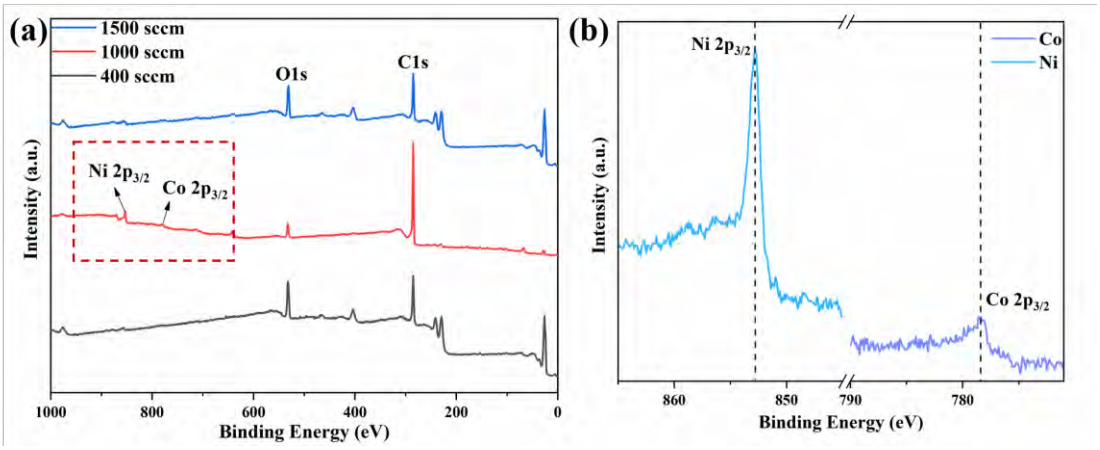

Fig. S3. (a) XPS survey spectra of hydrogenated graphene coatings deposited at different hydrogen supplies and (b) XPS Ni 2*p* and Co 2*p* spectra of hydrogenated graphene coatings deposited at a flow rate of 1,000 sccm. The peaks at 852.7 eV and 778.3 eV correspond to Ni $2p_{3/2}$ and Co $2p_{3/2}$ [1].

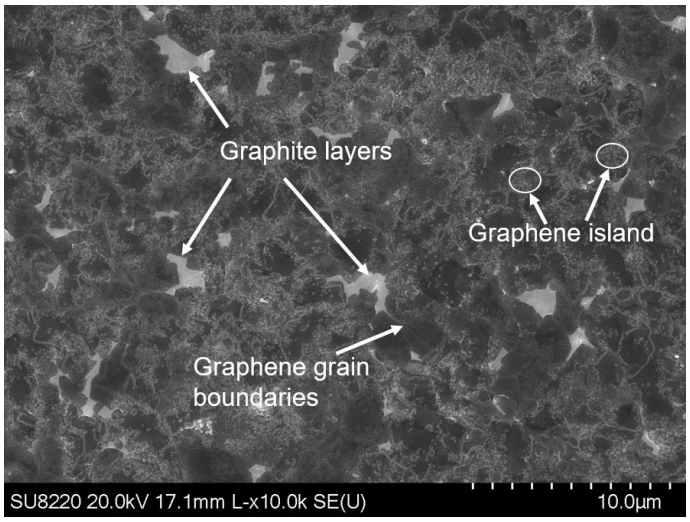

Fig. S4. SEM image (low magnification) of the hydrogenated graphene coating deposited at hydrogen supplies of 1,000 sccm. Since the growth of graphene follows the nucleation/growth and solution/precipitation mechanisms on a catalytic layer, the multi-oriented polycrystalline Ni-Co catalytic layer drives the growth of graphene coatings at different rates, resulting in regions with different numbers of coatings [2,3]. The graphene islands on the surface arise from the slow cooling rate which produces a deviation of C forming new graphene islands [4].

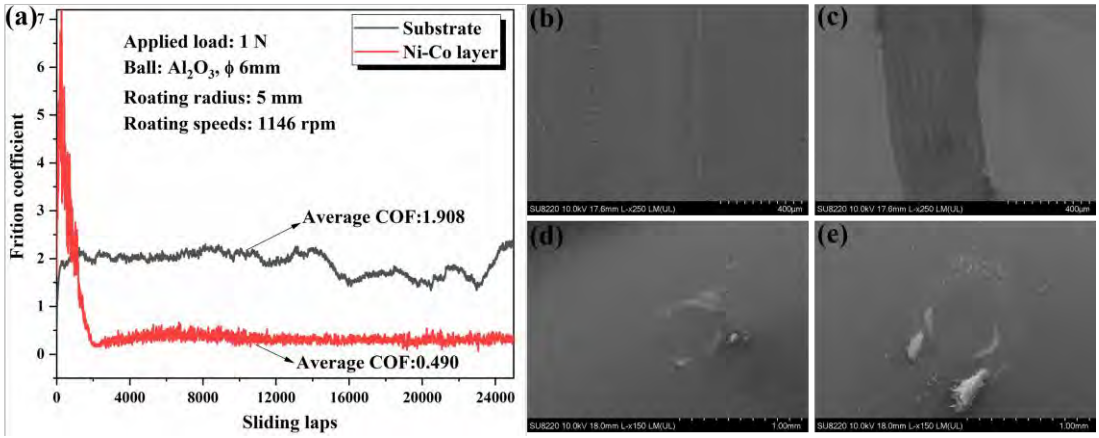

Fig. S5. Tribological properties of the substrate and Ni-Co layer samples. (a) Friction coefficient curve shows the average friction coefficients being 1.908 and 0.490 under a load of 1 N at 1,146 rpm (or 0.6 m/s). SEM image of the wear tracks and wear scars on the Al_2O_3 balls: (b, d) Substrate and (c, e) Ni-Co layer.

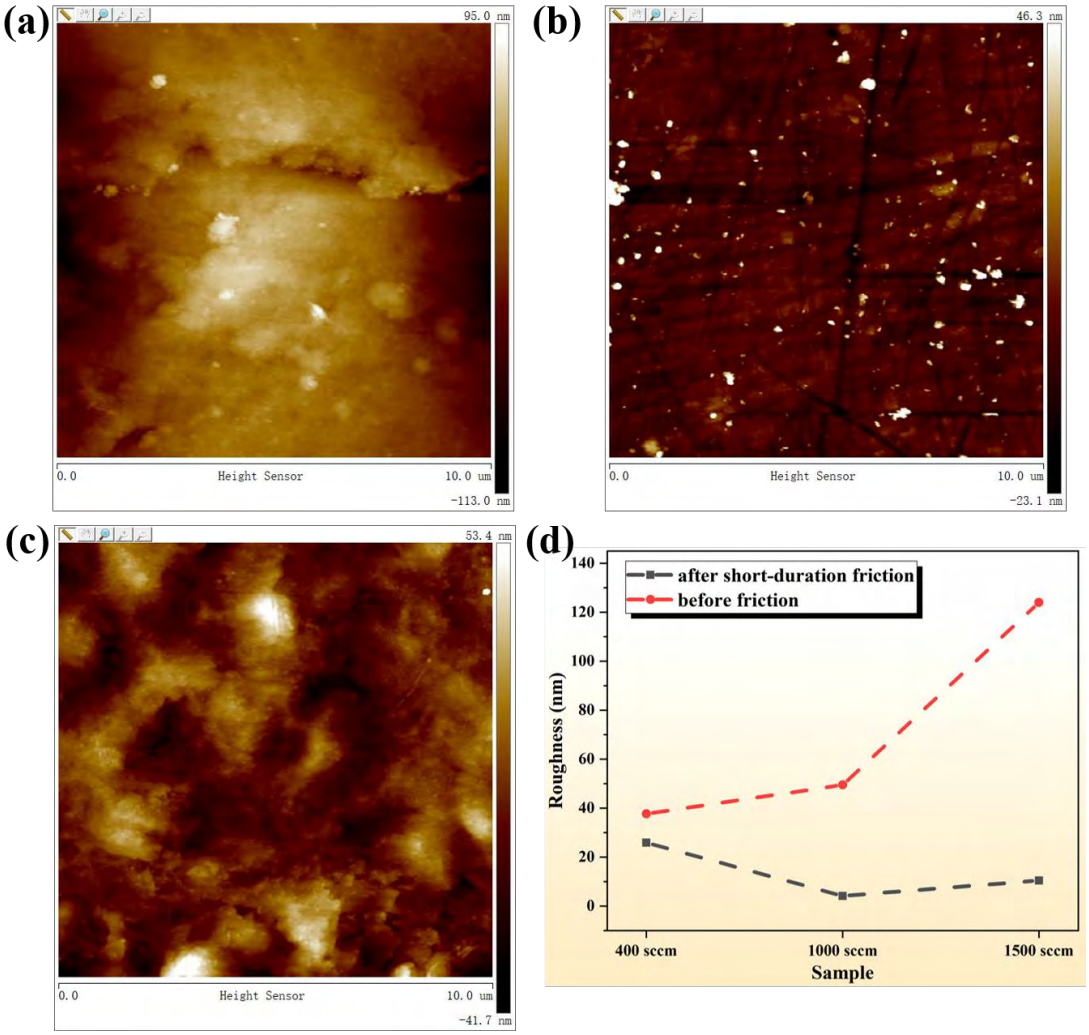

Fig. S6. Surface roughness change of the hydrogenated graphene coatings deposited at different hydrogen supplies after short-duration friction. Two-dimensional topographic images were taken from a 10×10 μm^2 area of the samples deposited at hydrogen supplies of (a) 400 sccm, (b) 1,000 sccm, and (c)1,500 sccm. (d) Comparison curve of Roughness change of wear track before and after short-duration friction.

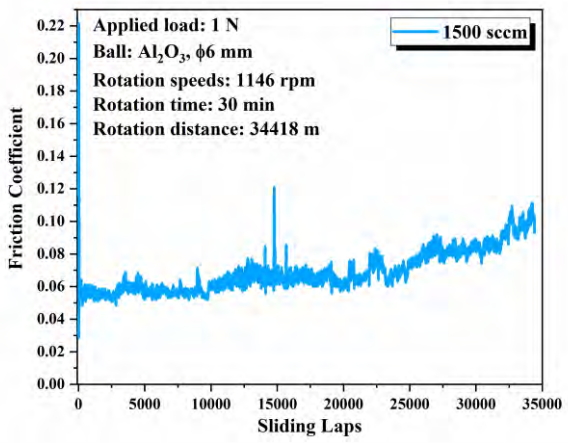

Fig. S7. Friction coefficient as a function of the hydrogenated graphene coatings deposited at 1,500 sccm hydrogen supplies during longer duration sliding.

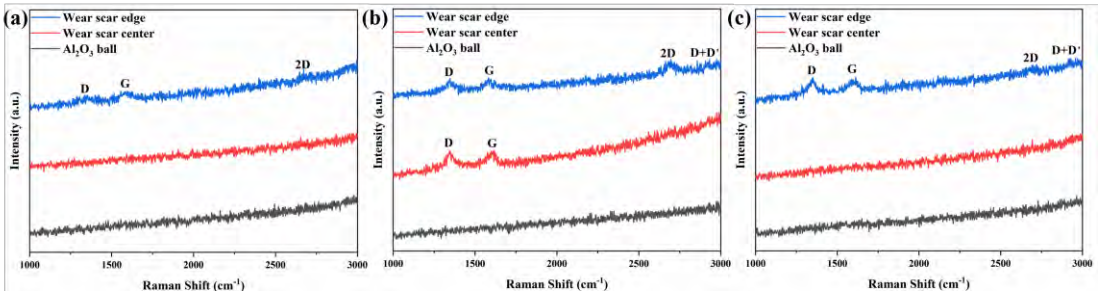

Fig. S8. Raman scattering spectra of the Al_2O_3 ball, wear scar edge, and center of the Al_2O_3 balls after the friction test of the hydrogenated graphene coatings deposited at different hydrogen supplies of (a) 400 sccm, (b) 1,000 sccm, and (c) 1,500 sccm.

Table S1. Molecular dynamics simulation parameters.

C atomic mass (g/mol)	12.0112
H atomic mass (g/mol)	1.00797
O atomic mass (g/mol)	15.9994
Al atomic mass (g/mol)	26.9820
Charge calculation cut-off radius (Å)	10
C-C bond length ι_{CC} (Å)	1.42
C-H bond length ι_{CH} (Å)	1.09

Table S2. Gaussian fitting results of the Raman spectra for different processing parameters.

	D (cm^{-1})	G (cm^{-1})	2D (cm^{-1})	I_D/I_G	I_{2D}/I_G	$2D_{FWHM}$ (cm^{-1})
400 sccm-Substrate	1348	1601	/	2.05	/	/
400 sccm-Ni-before annealing	1341	1585	/	1.96	/	/
400 sccm-Ni-after annealing	1344	1596	2658	1.80	0.37	103
1,000 sccm-Substrate	1359	1600	/	1	/	/
1,000 sccm-Ni-before annealing	1357	1588	2720	0.71	1.28	79
1,000 sccm-Ni-after annealing	1351	1588	2712	0.20	1.59	76
1,500sccm-Substrate	/	/	/	/	/	/
1,500 sccm-Ni-before annealing	1352	1590	2707	1.22	1.26	91
1,500 sccm-Ni-after annealing	1360	1591	2715	1.03	1.52	86

Table S3. The I_D/I_G values measured from the center and edge of the wear track on samples deposited with different strategies after short-duration and long-duration sliding.

Sliding test	Sample and area	I_D/I_G
Short-duration	400 sccm-center	1.90
	400 sccm-edge	1.67
	1,000 sccm-center	1.51
	1,000 sccm-edge	1.42
	1,500 sccm-center	1.65
	1,500 sccm-edge	1.63
Long-duration	400 sccm -center	2.40
	400 sccm-edge	1.65
	1,000 sccm-center	1.74
	1,000 sccm-edge	1.58
	1,500 sccm-center	1.95
	1,500 sccm-edge	1.61

Table S4. Chemical composition of the wear tracks on hydrogenated graphene coatings during the long friction.

	400 sccm sample	1,000 sccm sample	1,500 sccm sample
C (at.%)	18.5	23.21	25.04
O (at.%)	50.14	36.49	43.09
Ni (at.%)	31.46	33.33	30.74
Al (at.%)	/	1.06	1.14
Co (at.%)	/	5.91	/

Movie S1. Charge calculation motion path of slightly hydrogenated graphene layers.

Movie S2. Charge calculation motion path of highly hydrogenated graphene layers.

Supplementary References

[1] Y. Wang, P.J. Ren, J.T. Hu, Y.C. Tu, Z.M. Gong, Y. Cui, Y.P. Zheng, M.S. Chen, W.J. Zhang, C. Ma, L. Yu, F. Yang, Y. Wang, X.H. Bao, D.H. Deng, Electron penetration triggering interface activity of Pt-graphene for CO oxidation at room temperature, Nat. Commun. 12(1) (2021) 5814.

[2] X.S. Li, W.W. Cai, L. Colombo, R.S. Ruoff, Evolution of graphene growth on Ni and Cu by carbon isotope labeling, Nano Lett. 9(12) (2009) 4268-4272.

[3] T.R. Wu, X.F. Zhang, Q.H. Yuan, J.C. Xue, G.Y. Lu, Z.H. Liu, H.S. Wang, H.M. Wang, F. Ding, Q.K. Yu, X.M. Xie, M.H. Jiang, Fast growth of inch-sized single-crystalline graphene from a controlled single nucleus on Cu–Ni alloys, Nat. Mater. 15(1) (2016) 43-+.

[4] Y. Yang, G.L. Lu, Y.J. Li, Z.Z. Liu, X.Y. Huang, One-step preparation of fluorographene: a highly efficient, low-cost, and large-scale approach of exfoliating eluorographite, ACS Appl. Mater. Interfaces 5(24) (2013) 13478-13483.